

STAR FORMATION RATES AND EXTINCTION PROPERTIES OF IR-LUMINOUS GALAXIES IN THE *SPITZER* FIRST LOOK SURVEY

P. I. CHOI,¹ L. YAN,¹ M. IM,² G. HELOU,¹ B. T. SOIFER,¹ L. J. STORRIE-LOMBARDI,¹ R. CHARY,¹ H. I. TEPLITZ,¹ D. FADDA,¹ F. R. MARLEAU,¹ M. LACY,¹ G. WILSON,¹ P. N. APPLETON,¹ D. T. FRAYER,¹ AND J. A. SURACE¹

Received 2005 June 19; accepted 2005 September 27

ABSTRACT

We investigate the instantaneous star formation rates (SFRs) and extinction properties for a large ($N = 274$), near-infrared (NIR: $2.2 \mu\text{m}$) + mid-infrared (MIR: $24 \mu\text{m}$)-selected sample of normal to ultraluminous infrared galaxies (ULIRGs; $10^9 < L_{\text{IR}}/L_{\odot} < 10^{12.5}$) with $\langle z \rangle \sim 0.8$ in the *Spitzer* Extragalactic First Look Survey (FLS). We combine $24 \mu\text{m}$ observations with high-resolution Keck DEIMOS spectroscopy to derive optical emission-line ($\text{H}\alpha$, $\text{H}\beta$, and $[\text{O II}]$) and infrared star formation rates (SFR_{opt} and SFR_{IR} , respectively). Comparison of SFR diagnostics reveals a wide extinction range ($1.0 < A_V < 4.0$ mag) for this sample, even after removing spectroscopic and IRAC color-selected AGN candidates ($\approx 12\%$ of the sample). Objects with SFRs of a few $M_{\odot} \text{ yr}^{-1}$ have extinction values consistent with normal spirals ($A_V \approx 1.0$ mag). By contrast, LIRGs at $z \gtrsim 1$, which comprise a fraction of our sample, have $\text{SFR} \approx 100 M_{\odot} \text{ yr}^{-1}$ and a mean $A_V \approx 2.5$ mag. This translates to a 97% mean $[\text{O II}] \lambda 3727$ attenuation and in extreme cases is as high as 99.7%. We derive an IR-luminosity-dependent A_V^{IR} function [$A_V^{\text{IR}} = 0.75 \log(L_{\text{IR}}/L_{\odot}) - 6.35$ mag] that we use to extinction correct our line luminosities. The resulting correlation between SFR_{IR} and SFR_{opt} has a dispersion of ~ 0.2 dex (semi-interquartile range). Comparison of the A_V dependence on redshift and L_{IR} reveals that for a fixed L_{IR} , there is no significant A_V evolution. Comparison to previous studies reveals a mean attenuation that is intermediate between that of local optical/UV- and radio-selected samples with a marginally stronger L_{IR} dependence.

Subject headings: galaxies: bulges — galaxies: evolution — galaxies: high-redshift — galaxies: spiral — galaxies: starburst — infrared: galaxies

1. INTRODUCTION

Numerous investigations over the past decade have been directed at measuring the cosmic star formation history (SFH) of the universe. Observations over the full spectrum from radio to X-rays have been exploited to trace star formation rates (see Kennicutt 1998; Condon 1992; Ghosh & White 2001 for reviews of the various diagnostics). The most commonly used have historically been $\text{H}\alpha$ and $[\text{O II}]$ emission lines and UV continuum flux (e.g., Madau et al. 1996; Tresse & Maddox 1998; Hogg et al. 1998; Yan et al. 1999; Glazebrook et al. 1999; Adelberger & Steidel 2000; Wilson et al. 2002; Teplitz et al. 2003; Erb et al. 2003). This is largely due to their respective accessibility via ground-based observing windows for local and distant samples and the fact that they are relatively direct tracers of massive star formation. Unfortunately, optical and UV diagnostics are highly sensitive to dust attenuation. Various approaches have been implemented to estimate this reddening. The use of Balmer line flux ratios is a direct but observationally taxing method that requires high-resolution spectroscopy. In the absence of multiple well-measured emission lines, color- or magnitude-dependent optical extinction corrections (Rigopoulou et al. 2000; Hippelein et al. 2003) or the UV slope-extinction relation (β - A_{UV}) derived for starburst galaxies (e.g., Calzetti et al. 1994; Adelberger &

Steidel 2000) have also been adopted. Although commonly applied to nonstarburst galaxies, the latter has been shown to break down for both more and less luminous systems (Goldader et al. 2002; Bell et al. 2002; Bell 2002).

By comparison, far-infrared (FIR) and radio star formation rate (SFR) diagnostics have the advantage that they are unaffected by extinction. Their shortcoming, however, is that for general populations they have more complex relationships to the star formation than optical emission-line and UV indicators. For instance, the typically adopted FIR SFR calibration (Kennicutt 1998) is based on the assumption of infinite optical depth and 100% reprocessing of massive star UV emission into IR flux. This is a reasonable assumption for heavily extinguished systems, but breaks down for galaxies with moderate attenuation. In spiral galaxies, for instance, counteracting effects of UV radiation leakage and heating from older evolved stellar populations must also be considered (Lonsdale-Persson & Helou 1987). Finally, despite our relatively limited understanding of the decimeter radio continuum, it has served as a powerful proxy for the IR flux due to the tightness of radio-FIR correlation (Helou et al. 1985). Surprisingly, this correlation extends to IR luminosities ($\approx 0.01 L^*$) at which neither the bolometric infrared luminosity (L_{IR}) nor the radio continuum is reliably tracing star formation (Bell 2003).

Comparative studies of these different diagnostics exist for a range of galaxy types and sample selections. UV and $\text{H}\alpha$ measurements have been found to be generally consistent for local samples of normal galaxies (Sullivan et al. 2001, 2004; Bell & Kennicutt 2001; Buat et al. 2002). The scatter and, in some cases, the offset between the tracers are primarily attributed to a combination of uncertainties in the extinction correction, star/dust geometry, and the star formation timescale (Helou & Bicay 1993;

¹ *Spitzer* Science Center, California Institute of Technology, MS 220-6, Pasadena, CA 91125; pchoi@ipac.caltech.edu, lyan@ipac.caltech.edu, gkh@ipac.caltech.edu, bts@ipac.caltech.edu, lisa@ipac.caltech.edu, rchary@caltech.edu, hit@ipac.caltech.edu, fadda@ipac.caltech.edu, marleau@ipac.caltech.edu, mlacy@ipac.caltech.edu, gillian@ipac.caltech.edu, apple@ipac.caltech.edu, frayer@ipac.caltech.edu, jason@ipac.caltech.edu.

² Department of Astronomy, Seoul National University, Seoul, Korea; mim@astroim.snu.ac.kr.

Bell 2003; Sullivan et al. 2004). The intercomparison of UV/optical to decimeter radio emission (Sullivan et al. 2001; Afonso et al. 2003) and far-infrared *Infrared Astronomical Satellite (IRAS)* observations (Cram et al. 1998; Dopita et al. 2002; Kewley et al. 2002; Hopkins et al. 2003) for large local samples confirms the importance of accurate UV/optical attenuation corrections. Recent *Infrared Space Observatory (ISO)*-based studies by Rigopoulou et al. (2000), Cardiel et al. (2003), and Flores et al. (2004) probe out to more distant redshifts ($z \sim 1$) but for admittedly small samples of 12, 7, and 16 sources, respectively. These pioneering works provide the deepest IR-based SFR probes of the distant, dustier, and more actively star-forming universe. Consequently, they tend to include more extreme, IR-luminous galaxies than are present in the local samples.

Due to the absence of a unified multiwavelength picture of the SFH, there is considerable debate about the star formation density at high redshift. Most controversy revolves around issues of sample selection effects, SFR calibration uncertainties, and dust attenuation corrections. It has become clear that no single tracer is applicable for all galaxies. UV and optical diagnostics appear to be well suited for low IR luminosity galaxies that do not require significant extinction corrections, whereas attenuation-free IR and radio diagnostics provide better estimates in dusty, actively star-forming systems. In this work we study the star formation and extinction properties of a large, distant, actively star-forming population by making a direct comparison of optical emission-line and IR SFR diagnostics. Specifically, we use mid-IR observations from the *Spitzer* Extragalactic First Look Survey and deep Keck optical spectroscopic observations to achieve an order-of-magnitude increase in sample size over previous high-redshift *ISO* studies.

This paper is divided into the following sections. A summary of the various observational components and their basic analysis is given in § 2. Calculations of the optical and infrared star formation rates are described in § 3. Our approach for removing contaminating active galactic nuclei (AGNs) is outlined in § 4. The comparison between the optical and IR SFRs and our derived extinction corrections are discussed in § 5. The main points of this work are summarized in § 6. Throughout the paper, we adopt the cosmology of $\Omega_m = 0.27$, $\Omega_\Lambda = 0.73$, and $H_0 = 70 \text{ km s}^{-1} \text{ Mpc}^{-1}$.

2. OBSERVATIONS AND REDUCTIONS

The *Spitzer* extragalactic First Look Survey (FLS)³ region is a $\approx 4 \text{ deg}^2$ region centered around R.A. = $17^{\text{h}}18^{\text{m}}00^{\text{s}}$, decl. = $59^\circ30'00''$. It is chosen to lie within the continuous viewing zone (CVZ), to have minimum cirrus and no bright radio sources. Observations of this field with each of the four Infrared Array Camera (IRAC) and three Multiband Imaging Photometer for *Spitzer* (MIPS) imaging bands were one of the first science tasks undertaken by *Spitzer*. In addition to IR imaging, numerous ancillary data sets including radio, optical, and near-IR (NIR) data have been taken in this field. Brief descriptions of the data sets included in this study are given below.

2.1. Imaging

2.1.1. Optical

Optical *R*-band imaging of the FLS was carried out using the MOSAIC-I camera on the 4 m Mayall Telescope at the Kitt

Peak National Observatory (KPNO) on four consecutive nights on UT 2000 May 4–7. A 4×2 array of SITe 2048×4096 CCDs provides a $36' \times 36'$ field of view with a $0''.258$ pixel scale. Tiling 26 individual pointings, we obtain an *R*-band coverage of 9.4 deg^2 , with a median exposure time per pointing of 1800 s and typical seeing of $\text{FWHM} \sim 1''.0$. The resulting source catalog has a 50% completeness limit of $R = 24.5$ mag (Vega). In addition, *g'*- and *i'*-band observations of the FLS were obtained using the Large Format Camera (LFC) on the 200 inch (5.1 m) Palomar Observatory Hale Telescope. These observations were taken over multiple observing campaigns from 2001 August through 2004 June. The total area coverage in these bands is roughly 2.0 deg^2 , with comparable seeing and resolution to that of the *R*-band data. Comprehensive descriptions of these data sets are presented in Fadda et al. (2004) and T. M. Glassman et al. (2006, in preparation).

2.1.2. Near-Infrared

Near-infrared observations were carried out in two separate but complementary observing campaigns that can be characterized as shallow, wide field and deep, narrow field. In the first, K_s -band imaging of a 1.14 deg^2 region, to a median depth of $K_s < 19.0$ mag (Vega), was performed on UT 2001 May 23–26 using the Florida Multiobject Imaging Near-IR Grism Observational Spectrometer (FLAMINGOS) on the Kitt Peak National Observatory 2.1 m telescope. A 2048×2048 HgCdTe Rockwell array provides a $20' \times 20'$ field of view with a $0''.6$ pixel scale. Each pointing was composed of 50 30 s exposures taken in a 25 position dither pattern. The field was mapped with a 5×5 grid pattern using half-field offsets ($10'$) between pointings. The median exposure time is $2400 \text{ s pixel}^{-1}$, and the median stellar point-spread function over the mosaic is $\text{FWHM} = 1''.6$.

In addition to the KPNO data set, a smaller $\approx 45' \times 45'$ verification region in the center of the FLS was observed with the Wide-Field Infrared Camera (WIRC) on the Palomar Observatory Hale 200 inch (5.1 m) telescope. Observations were undertaken over the course of multiple observing runs between 2002 June and 2004 July. A 2048×2048 Hawaii-II HgCdTe array provides an $8''.7 \times 8''.7$ field of view with a $0''.25$ pixel scale. The $\approx 0.6 \text{ deg}^2$ area centered on the FLS verification region was covered with 34 tiled pointings. The average exposure time per pointing is 3600 s (120×30 s) taken with a 30 position random dither pattern, to a median depth of $K_s < 20.2$ mag (Vega). A detailed description of all of the NIR observations and reductions is presented in T. M. Glassman et al. (2006, in preparation).

2.1.3. Mid-Infrared

The extragalactic component of the *Spitzer* FLS comprises IRAC (Fazio et al. 2004) and MIPS (Rieke et al. 2004) observations taken in 2003 December with a total exposure time of 63 hr. The MIPS $24 \mu\text{m}$ area coverage was 4.4 deg^2 for the main field and 0.26 deg^2 in a deeper verification field, with respective 3σ depths of 0.11 and 0.08 mJy. All data were processed and stacked by the data processing pipeline at the *Spitzer* Science Center (SSC). MIPS photometry was performed using StarFinder (Diolaiti et al. 2000), which measures profile-fit fluxes for point sources. A complete description of the $24 \mu\text{m}$ data reduction and source catalog can be found in Marleau et al. (2004) and D. Fadda et al. (2006, in preparation).

2.2. Spectroscopy

Optical spectroscopy was obtained with the Deep Imaging Multi-Object Spectrograph (DEIMOS; Faber et al. 2003) on the W. M. Keck II 10 m telescope. Observations were performed over three nights from UT 2003 June 27 to 29. A 1200 line mm^{-1}

³ For details of the FLS observation plan and the data release, see <http://ssc.spitzer.caltech.edu/fls>.

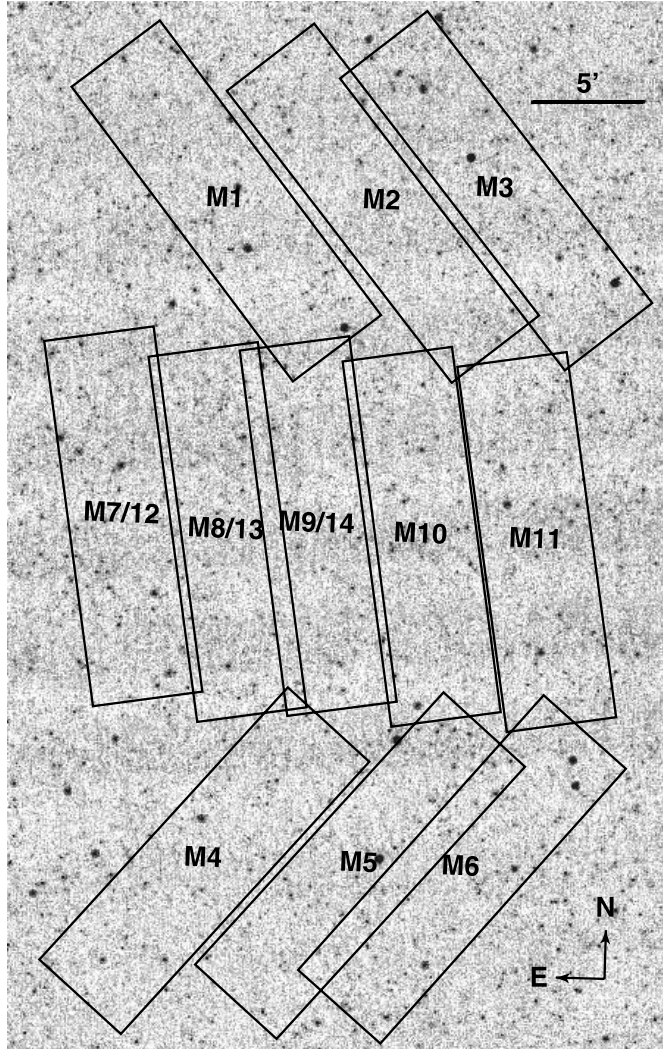


FIG. 1.—MIPS 24 μm image of the central 30' \times 45' region of the First Look Survey verification region. Positions of 14 5' \times 17' Keck DEIMOS optical spectroscopy slit masks are shown. A summary of the spectroscopic observations is given in Table 1.

grating with central wavelength settings of 7400 and 7699 \AA was used with the GG495 blocking filter, resulting in a 0.33 \AA pixel $^{-1}$ mean spectral dispersion and a 1.45 \AA instrumental resolution. The total spectral range observed was 6300–9300 \AA ; however, the coverage for an individual source was limited to 2630 \AA with a slit-position-dependent starting wavelength.

A total of 14 multislit masks were observed, with ≈ 100 1'' wide slits per mask. The 5' \times 16' slit masks were tiled in 11 unique positions to sample a 25' \times 45' area centered on the FLS. In Figure 1, mask positions are shown on top of the 24 μm mosaic for illustration. Multiple masks were observed for three of the positions in the deepest central region. Table 1 lists the positions, position angles (P.A.), and exposure times for the 14 observed masks.

We require minimum slit lengths of 7'' for local sky subtraction and adopt the Deep Extragalactic Evolutionary Probe 2 (DEEP2) recommended strategy of using tilted slits to better sample and remove sky lines. Slit position angles θ were required to be $10^\circ < |\theta| < 25^\circ$ from the spatial axis and, when possible, were positioned along the major axes of elongated galaxies. Of the 14 masks, three were observed for a total of 10,800 s (3×3600 s), and the remaining 10 masks were observed for a

TABLE 1
SPECTROSCOPIC OBSERVATION LOG

ID	R.A. (J2000.0)	Decl. (J2000.0)	P.A. (deg)	Exposure Time (minutes)
M1	17 17 08.51	59 59 53.5	-39	3 \times 20
M2	17 16 11.74	60 00 02.3	-40	3 \times 20
M3	17 15 30.86	60 00 46.0	-40	3 \times 20
M4	17 17 07.65	59 29 58.6	40	3 \times 20
M5	17 16 12.00	59 30 00.0	40	3 \times 20
M6	17 15 35.57	59 29 58.8	39	3 \times 20
M7	17 17 41.53	59 45 26.1	-10	5 \times 45
M8	17 17 03.68	59 45 00.0	-10	4 \times 45
M9	17 16 31.14	59 45 24.8	-10	4 \times 45
M10	17 15 53.81	59 45 05.2	-10	3 \times 20
M11	17 15 12.35	59 45 00.6	-10	3 \times 20
M12	17 17 41.39	59 45 32.0	-10	3 \times 20
M13	17 17 03.68	59 45 00.0	-10	3 \times 20
M14	17 16 31.14	59 45 24.8	-10	3 \times 20

NOTE.—Units of right ascension are hours, minutes, and seconds, and units of declination are degrees, arcminutes, and arcseconds.

total of 3600 s (3×1200 s). Observing conditions over the course of the run were good, with a typical seeing of FWHM $\sim 0''.7$. For data reduction, we employ the DEEP2 spec2d pipeline,⁴ which is based on the Sloan Digital Sky Survey (SDSS) spectral reduction package. This package performs cosmic-ray removal, flat-fielding, co-addition, sky subtraction, wavelength calibration, and both two-dimensional and one-dimensional spectral extraction.

2.2.1. Emission-Line Measurements and Redshift Identification

The one-dimensional spectral output of the DEEP2 pipeline is analyzed using an in-house IDL package written by P. I. C. and D. F. Galaxy redshifts are identified through visual inspection and galaxy template cross-correlation. Line flux, equivalent width, and kinematic measurements are made by performing Gaussian profile fits to the one-dimensional spectra. This is done interactively with the user identifying the lines to be fit and specifying the spectral region over which to perform the line + continuum fit. Our high spectral resolution (1.45 \AA instrumental resolution) allows for most lines to be modeled individually. One exception is the [O II] doublet $\lambda\lambda 3726, 3729$, which is unresolved in $\approx 1/2$ of our sample. Rather than measure each line independently, we adopt a double Gaussian profile with a fixed line separation of $(1+z)2.75$ \AA . We require the two lines to have the same FWHM, but allow their flux ratio to be a free parameter.

In the case of Balmer line fits, two-component emission + absorption profiles are adopted. It is well known that nebular Balmer emission lines can suffer from contamination due to underlying stellar absorption and subsequently be underestimated. The standard technique to correct for stellar absorption is to apply a global Balmer line equivalent width correction. Fortunately, our high spectral resolution enables us to resolve and directly measure the nebular emission and the pressure-broadened stellar absorption components. This eliminates the need for a global correction and results in more accurate line fluxes. Figure 2 provides an illustration of two typical emission-line fits. Figure 2a shows a double Gaussian line fit to the [O II] $\lambda\lambda 3727$ doublet, while Figure 2b shows an emission + absorption two-component fit to H β .

⁴ See <http://astron.berkeley.edu/~cooper/deep/spec2d>.

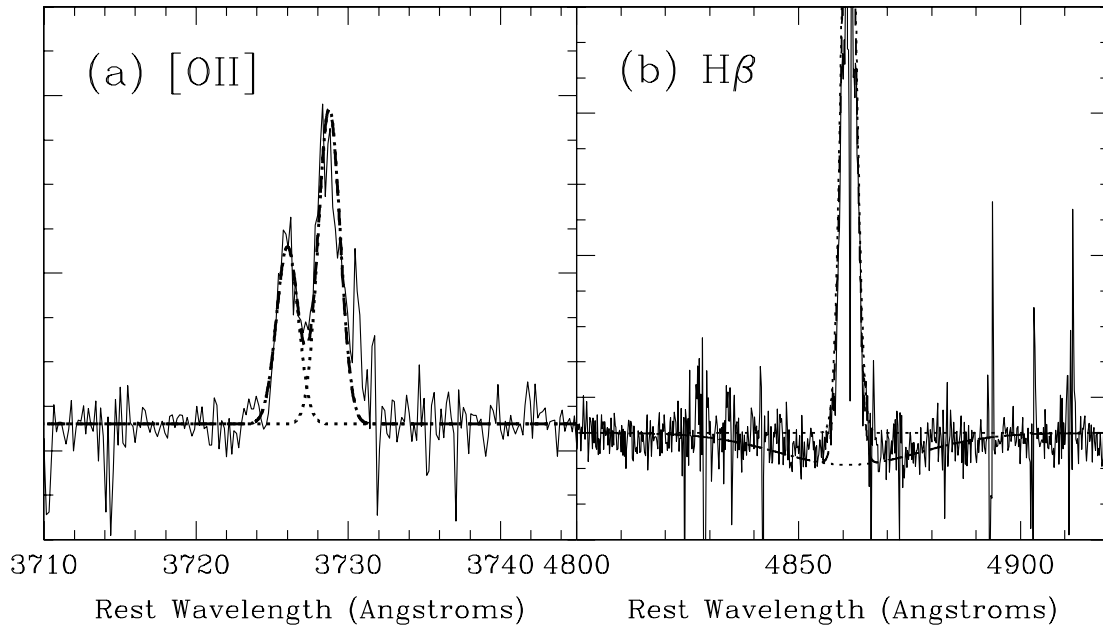


FIG. 2.—Line fits of [O II] and H β for two representative objects in our sample. (a) [O II] $\lambda\lambda 3727$ doublet. The Gaussian profiles of the individual lines (dotted lines) are shown along with their co-addition (dashed line). The lines are required to have the same FWHM and a fixed 2.75 Å *rest-frame* separation. (b) Individual components (dotted lines) and the co-added H β line fit (dashed line).

2.2.2. Final MIR + NIR Sample

The spectroscopic observations were designed to target a flux-limited NIR-selected sample based primarily on our K_s -band data set. Optical g' -, R -, and i' -band color information was included exclusively to (1) clean out stellar contaminants and (2) apply a rough photometric redshift selection, designed to prioritize high-redshift sources with $z > 0.6$. The detailed description of this color selection will be discussed separately in the spectroscopic catalog paper.

The final sample used for this study includes all galaxies in our spectroscopic sample with a high-confidence redshift and a significant 24 μ m detection. In Figure 3, the full NIR-selected sample with good spectroscopic redshifts (*solid line*) is shown

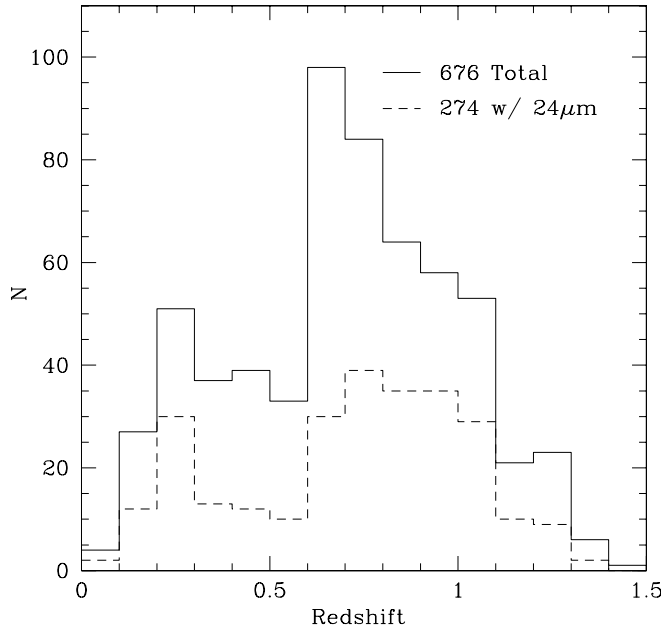


FIG. 3.—Spectroscopic redshift distribution of our full 676 galaxy sample (*solid line*) and the 274 galaxy, 24 μ m-detected subsample (*dashed line*).

in contrast to the subsample that has 24 μ m-detected counterparts (*dashed line*).

The effect of our g' , R , i' , and K_s color selection is seen in both distributions as a sharp drop-off below $z < 0.6$. Beyond $z > 1.1$, the impact of our decreasing spectroscopic redshift sensitivity is evident. In this regime strong sky lines make it challenging to cleanly identify [O II] $\lambda\lambda 3726, 3729$. By $z > 1.3$, this feature has moved out of our spectral coverage window for much of our sample. The final $K_s + 24 \mu$ m sample includes 274 galaxies and has a median redshift of $\bar{z} = 0.76$.

To investigate how our spectroscopic redshift target selection is biasing our NIR + MIR distribution, we show in Figure 4

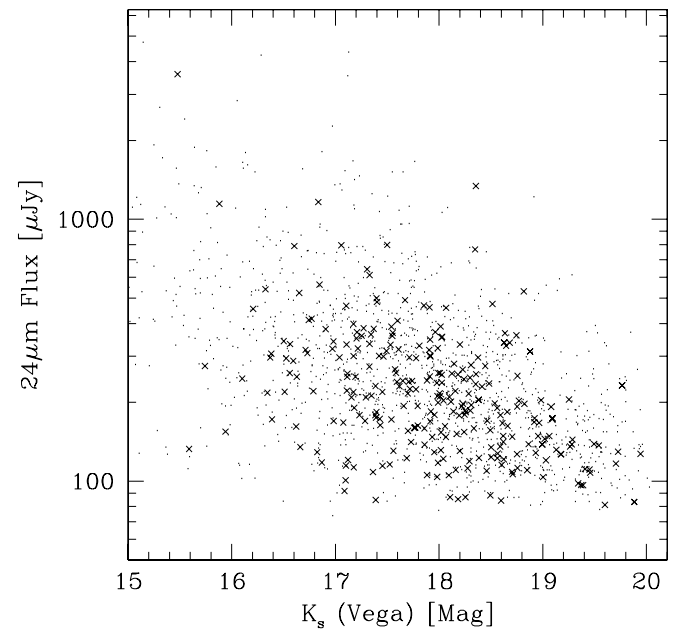


FIG. 4.—MIPS 24 μ m flux vs. K_s -band magnitude for the spectroscopic (*crosses*) and parent photometric (*dots*) samples. Comparison of the two distributions illustrates that the parent population is being reasonably well represented with our spectroscopic sample for all but the brightest sources ($K_s > 16.5$ mag).

the K_s versus 24 μm flux for the parent photometric sample (*dots*) and the targeted spectroscopic sample (*crosses*). Our selection against low-redshift sources is evidenced in this distribution by the lack of NIR-bright ($K_s < 16.5$ mag) spectroscopic targets.

3. SFR COMPUTATIONS

3.1. Emission-Line SFR Diagnostics

The $\text{H}\alpha \lambda 6563$ emission line is the most prominent and often measured SFR diagnostic in local galaxy surveys. Unfortunately, at even moderate redshifts ($z \gtrsim 0.4$) this line becomes observationally taxing, as it moves first into the forest of OH sky lines and then beyond the optical spectral window. Higher order Balmer lines such as $\text{H}\beta$ and $\text{H}\gamma$ can be related to $\text{H}\alpha$; however, these are often overlooked because their weak line strength and contamination from underlying stellar absorption make them difficult to measure. At redshifts where all the prominent Balmer lines become inaccessible ($z \gtrsim 0.9$), the $[\text{O II}]$ doublet $\lambda\lambda 3727$ can be used based on the $\text{H}\alpha/[\text{O II}]$ line ratio. For this study, we use a combination of all these lines to track the SFR over the redshift range of our sample. $\text{H}\alpha$, $\text{H}\beta$, and $[\text{O II}]$ are measured for galaxies in the respective redshift ranges $z \lesssim 0.4$, $0.3 \gtrsim z \gtrsim 0.9$, and $z \gtrsim 0.7$. When accessible, $\text{H}\gamma$ and $\text{H}\delta$ are also used as secondary diagnostics. In this section, we discuss the flux measurement and SFR conversion for each of these lines.

3.1.1. Line Luminosity Measurement

The most direct approach for measuring the total emission-line flux of a galaxy is direct integration of a flux-calibrated spectrum. Unfortunately, this is impractical for many surveys, given the challenges of properly flux calibrating large multislit samples. An alternate route is to combine line equivalent widths with broadband photometry (e.g., Hogg et al. 1998; Hopkins et al. 2003). In our case, we compute k -corrected absolute u' , g' , and R -band magnitudes using our observed g' , R , i' , and K_s photometry and the KCORRECT code (Blanton et al. 2003), adapted for our data set. We adopt these rest-frame magnitudes as approximations of the continuum flux density at the rest wavelengths of $[\text{O II}]$, $\text{H}\beta$, and $\text{H}\alpha$ (3727, 4861, and 6563 \AA , respectively). Luminosities of these emission lines are then given by

$$L_{\text{H}\alpha} = \text{EW}_{\text{H}\alpha} 10^{[-0.4(M_R - 34.10)]} \frac{3.0 \times 10^{18}}{\lambda_{\text{rest}}^2} (\text{W}), \quad (1)$$

$$L_{\text{H}\beta} = \text{EW}_{\text{H}\beta} 10^{[-0.4(M_{g'} - 34.10)]} \frac{3.0 \times 10^{18}}{\lambda_{\text{rest}}^2} (\text{W}), \quad (2)$$

$$L_{[\text{O II}]} = \text{EW}_{[\text{O II}]} 10^{[-0.4(M_{u'} - 34.10)]} \frac{3.0 \times 10^{18}}{\lambda_{\text{rest}}^2} (\text{W}), \quad (3)$$

where EW is the line equivalent width in angstroms, M is the k -corrected absolute AB magnitude appropriate for the rest wavelength of the line being measured, and λ_{rest} is the central wavelength of the broadband filter, also in angstroms. These derivations assume that the continuum flux at a given emission-line wavelength is well approximated by the flux density at the corresponding broadband effective wavelength. An additional color correction can be made to account for the wavelength difference between the line and the filter effective wavelength; however, we find this correction to be negligibly small (of the order of a few percent), so it is excluded.

A major benefit of this approach is that it alleviates the need for aperture/slit corrections that can plague direct flux measurements. These corrections are small for compact galaxies, but can be substantial for extended sources. Consequently, aperture loss tends to be redshift dependent and has the potential to masquerade as evolution. By contrast, line equivalent widths and the scaled line fluxes described above are fairly insensitive to slit loss. This approach does rely on the underlying assumption that the average line-to-continuum ratio within the slit is the same as that outside the slit; however, the same assumption is made when correcting for slit loss.

3.1.2. Balmer Line SFR Diagnostics

The Balmer line star formation rate diagnostics rely on the $\text{H}\alpha$ -SFR calibration derived by Kennicutt (1998),

$$\text{SFR}_{\text{H}\alpha} = 7.90 \times 10^{-42} L_{\text{H}\alpha} E_{\text{H}\alpha} (\text{ergs s}^{-1}), \quad (4)$$

where $L_{\text{H}\alpha}$ is the measured line luminosity and $E_{\text{H}\alpha}$ is the extinction correction factor, measured at the wavelength of $\text{H}\alpha$. This correlation is based on evolutionary synthesis models assuming solar abundance, a Salpeter initial mass function (IMF) with stellar mass limits of $0.1 < M < 100 M_\odot$, and $T_e = 10,000$ K case B recombination. It also assumes that the escape fraction of ionizing radiation from the observed galaxy is negligible and therefore that the nebular emission traces all of the massive star formation.

The conversion for higher order Balmer lines is derived based on the intrinsic case B recombination line ratios. As discussed in § 2.2.1, these lines tend to be less frequently adopted as SFR tracers due to the difficulties of properly correcting for stellar absorption; however, Kennicutt (1992) has shown that even with the adoption of a mean correction, for strong emission-line galaxies $\text{H}\beta$ can be a reliable SFR diagnostic. Incorporating the expected $\text{H}\alpha/\text{H}\beta = 2.87$ line ratio (Osterbrock 1989), we obtain the relation for $\text{SFR}_{\text{H}\beta}$,

$$\text{SFR}_{\text{H}\beta} = 2.75 \times 10^{-42} L_{\text{H}\beta} E_{\text{H}\beta} (\text{ergs s}^{-1}), \quad (5)$$

where the extinction term $E_{\text{H}\beta}$ is measured at $\text{H}\beta$. Similar relations for $\text{H}\gamma$ and $\text{H}\delta$ are derived based on the $\text{H}\gamma/\text{H}\beta = 0.466$ and $\text{H}\delta/\text{H}\beta = 0.256$ line ratios.

3.1.3. $[\text{O II}]$ Forbidden Line SFR Diagnostic

For the most distant $z \gtrsim 0.7$ sources in our sample, we compute the SFR based on the $[\text{O II}] \lambda\lambda 3727$ forbidden line doublet, adopting the Kewley et al. (2004) calibration,

$$\text{SFR}_{[\text{O II}]} = (0.66 \pm 0.17) \times 10^{-41} L_{[\text{O II}]} E_{[\text{O II}]} (\text{ergs s}^{-1}). \quad (6)$$

Following the notation above, $L_{[\text{O II}]}$ is the measured line luminosity and $E_{[\text{O II}]}$ is the extinction correction factor at $\lambda 3727$. An important difference with respect to most previous $[\text{O II}]$ calibrations is that equation (6) does not include any assumptions about the differential reddening between $\text{H}\alpha$ and $[\text{O II}]$ of the source. By contrast, the standard conversion of Kennicutt (1998, 1992; cf. Gallagher et al. 1989),

$$\text{SFR}_{[\text{O II}]} = (1.4 \pm 0.4) \times 10^{-41} L_{[\text{O II}]} E_{\text{H}\alpha} (\text{ergs s}^{-1}), \quad (7)$$

requires the calibration of a mean reddening between $\text{H}\alpha \lambda 6563$ and $[\text{O II}] \lambda\lambda 3727$. The assumption of an average $\text{H}\alpha$ to $[\text{O II}]$ reddening is reasonable for samples with a narrow range of intrinsic extinction; however, it would lead to systematic,

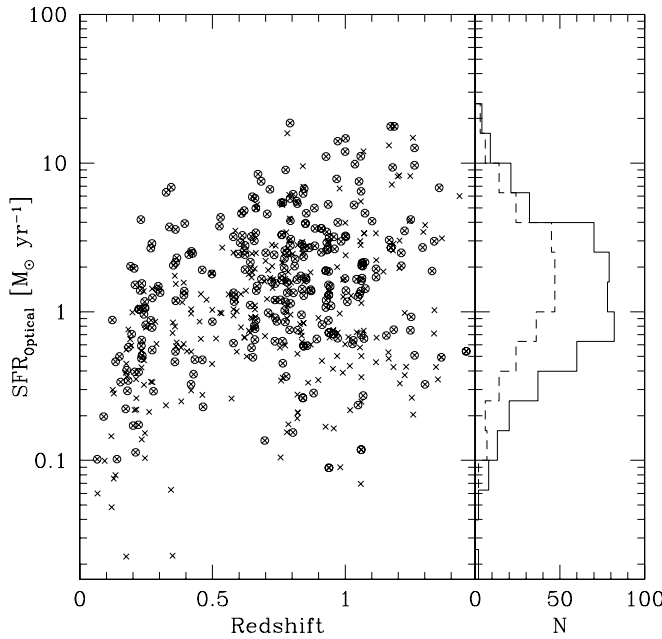


FIG. 5.—Extinction-uncorrected emission-line-derived SFR_{opt} vs. redshift for the full 676 galaxy, NIR-selected sample (crosses) and the 274 galaxy, $K_s + 24 \mu\text{m}$ -detected subset (circles). The integrated SFR_{opt} distributions of the full (solid line) and $24 \mu\text{m}$ -detected (dashed line) samples show that the mean SFR_{opt} for IR-luminous sources is higher than that of the parent population. The lack of a clean separation between the detected and nondetected sources is an expected consequence of an L_{IR} -dependent optical extinction.

extinction-dependent errors for more general samples with broad $E(B - V)$ distributions. In addition, since the current sample has a considerably brighter mean IR luminosity than those of the Kennicutt (1992) or Gallagher et al. (1989) calibration data sets, using equation (7) would tend to underestimate both the total $[\text{O II}]$ extinction and star formation rate.

It is worth noting that equation (6) ignores metallicity effects on the $[\text{O II}]$ to Balmer line luminosity ratio. Kewley et al. (2004) do characterize the abundance dependence of this ratio; however, due to our lack of metallicity measurements, we use their $SFR_{[\text{O II}]}$ calibration that adopts a mean abundance value of the Nearby Field Galaxy Survey (NFGS). Although a detailed investigation of this issue is beyond the scope of this work, we can use their findings to estimate the impact of metal abundance on our derived SFRs. Over the metallicity range $8.0 < \log(\text{O/H}) + 12 < 9.0$ (based on the McGaugh [1991] R_{23} calibration) of the NFGS sample, Kewley et al. (2004) find that the $[\text{O II}]/\text{H}\alpha$ ratio exhibits a metallicity-dependent range of ± 0.2 dex. The adoption of a mean abundance introduces $\lesssim 0.08$ dex of scatter into their $[\text{O II}]/\text{H}\alpha$ correlation. We expect a comparable impact on the scatter of our $SFR_{[\text{O II}]}$ diagnostic. At that level, it does not have a significant effect on our $SFR_{[\text{O II}]}$ or extinction uncertainties.

Finally, in Figure 5 we combine the above emission-line diagnostics to look at the optically derived, extinction-uncorrected SFR versus redshift. Comparison of the parent NIR-selected sample with the $24 \mu\text{m}$ -detected subsample reveals that the latter has a higher mean uncorrected SFR_{opt} . This is not an unexpected result, since IR flux traces star formation. A bit surprising is the degree of overlap between the SFR_{opt} distributions of IR-detected and nondetected sources. The fact that at any given redshift, SFR_{opt} (uncorrected) provides little indication of whether a source will be IR luminous or not suggests an IR-luminosity-dependent attenuation.

3.2. IR SFR Calculations

An alternative SFR tracer that is unaffected by extinction is the infrared luminosity. The IR component of galaxy spectral energy distributions (SEDs) can be decomposed into three main dust emission components: (1) a near blackbody emission profile of a thermally heated “cold” big grain (BG) dust component, (2) a near blackbody component of a stochastically heated “warm” very small grain (VSG) dust, and (3) molecular polycyclic aromatic hydrocarbon (PAH) emission features (Desert et al. 1990; Dale & Helou 2002, hereafter DH02). The primary heat sources for these dust components are stellar radiation from young stars, an older evolved stellar population, and AGNs.

In dusty, high-opacity systems, where the dominant heat source of the IR dust radiation is young stars (i.e., starbursts and LIRGs), the IR luminosity is expected to be an excellent tracer of the instantaneous SFR. In these situations, the conversion of L_{IR} to a star formation rate can be made with the calibration of Kennicutt (1998),

$$SFR_{\text{IR}} = 4.5 \times 10^{-44} L_{\text{IR}} \text{ (ergs s}^{-1}\text{)}, \quad (8)$$

where L_{IR} is defined as the integrated luminosity from 8 to $1000 \mu\text{m}$.⁵ Equation (8) is based on the assumption of solar abundance, a Salpeter IMF ($0.1-100 M_{\odot}$), and an optically thick dust distribution. It is consistent ($\pm 30\%$) with published calibrations of comparably selected samples (Kennicutt 1998); however, its extension to more general galaxy populations should be made with caution. Specifically, the assumption of high optical depth places an important limitation on its application to normal spiral galaxies. Large UV/optical escape fractions, whether due to low dust opacity or dust/star geometry, will cause SFR_{IR} to underestimate the true SFR. On the other hand, heating of the diffuse interstellar medium (ISM) by an older background population can contribute significantly to the IR luminosity (Lonsdale-Persson & Helou 1987; Helou 2000), resulting in an overestimate of the SFR. At the high IR luminosity extreme, the SFR_{IR} calibration runs into the problem that many ULIRGs derive a significant fraction of their bolometric luminosity from AGNs. In these systems, dust heating from a central AGN can be the dominant component of L_{IR} . This contribution is difficult to quantify, so it is essential to screen these sources. In § 4 we discuss our approach for removing AGNs from our sample.

3.2.1. Bolometric Correction

To calculate SFR_{IR} , we first compute the bolometric IR luminosity from our $24 \mu\text{m}$ observations. A standard approach for deriving L_{IR} for local galaxies is to use the definition of Sanders & Mirabel (1996), based on $IRAS$ 12, 25, 60, and $100 \mu\text{m}$ luminosities,

$$\begin{aligned} L_{\text{IR}}[8-1000 \mu\text{m}] &= 1.8 \times 10^{-14} \times 10^{26} [13.48 L_{\nu}(12) \\ &\quad + 5.16 L_{\nu}(25) + 2.58 L_{\nu}(60) + L_{\nu}(100)], \end{aligned} \quad (9)$$

where $L_{\nu}(\lambda)$ is in units of $L_{\odot} \text{ Hz}^{-1}$ and L_{IR} is in units of L_{\odot} . A comparable $Spitzer$ band transformation exists (DH02); however, its application for distant galaxies is hindered by the general dearth of multiband FIR photometry. For instance, the bulk of our FLS sample is observed but undetected with 70 and $160 \mu\text{m}$ imaging. Fortunately, it has been shown from $IRAS$ and ISOCAM

⁵ NB: Different authors have conflicting definitions for L_{IR} and L_{FIR} .

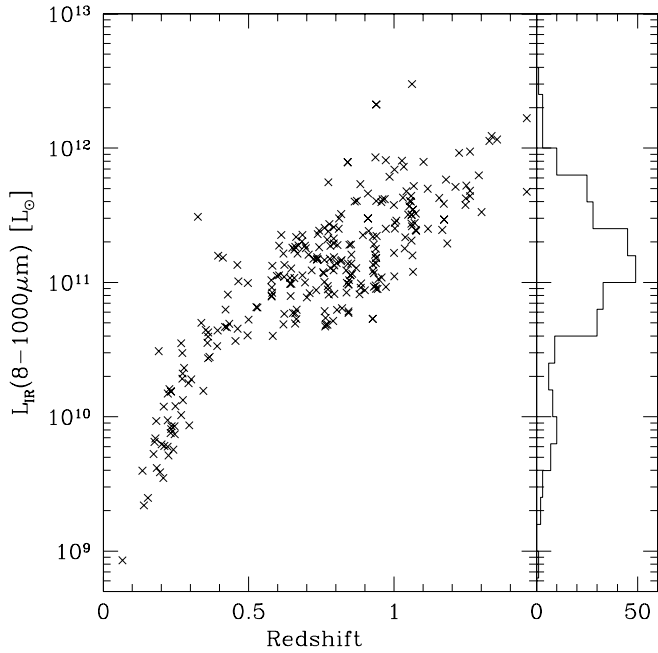


FIG. 6.—Plot of L_{IR} vs. redshift for our full ($N = 274$) $K_s + 24 \mu\text{m}$ -detected sample with accurate spectroscopic redshifts. The L_{IR} distribution is also shown in the right panel.

data that the MIR alone is a reasonable tracer of L_{IR} (Elbaz et al. 2002; Takeuchi et al. 2005). We exploit this finding and use our $24 \mu\text{m}$ observations, which correspond to rest-frame $10\text{--}24 \mu\text{m}$ over the redshift range of our sample, to derive IR luminosities.

Rather than implement a single L_{MIR} to L_{IR} correlation, we take the approach of using template SEDs (Chary & Elbaz 2001, hereafter CE01) to derive $L_{\text{IR}}(8\text{--}1000 \mu\text{m})$ from the $24 \mu\text{m}$ fluxes. CE01 have constructed a library of 105 flux-calibrated SEDs that are single valued in L_{IR} and cover the spectral range $0.1\text{--}1000 \mu\text{m}$. They start with model SEDs matched to a sample of local galaxies ranging from a normal spiral (M51) to a ULIRG (Arp 220; Silva et al. 1998) and combine them with MIR ISOCAM spectra and FIR model SEDs. They then split and recombine the MIR and FIR components of these templates to create a library of SEDs that reproduce the observed correlations between the various *IRAS*, ISOCAM, and Submillimeter Common-User Bolometric Array (SCUBA) IR fluxes of local galaxies. We implement these templates in a manner described by Elbaz et al. (2002) as the “multitemplate” approach. For each galaxy in our sample, we shift the template SEDs to the redshift of that source. We choose the template that most closely reproduces the observed $24 \mu\text{m}$ flux and use its 12, 25, 60, and $100 \mu\text{m}$ integrated fluxes to compute $L_{\text{IR}}(8\text{--}1000 \mu\text{m})$ based on equation (9). The final distribution of L_{IR} for the $K_s + 24 \mu\text{m}$ -detected sample is shown in Figure 6. This plot of L_{IR} versus redshift reveals that our sample spans a broad range in both L_{IR} and redshift but is strongly concentrated around $L_{\text{IR}}/L_{\odot} \approx 2.0 \times 10^{11}$ and $z \approx 0.8$. In addition, as a consequence of our $24 \mu\text{m}$ flux limit, L_{IR} and redshift are correlated. The impact of this correlation on our results is discussed further in § 5.2.3.

It should be noted that the application of this CE01 SED library relies on the assumption that the luminosity trends seen locally are representative of our sample, at higher redshift. This has been shown to be reasonable at least out to $z \sim 0.8$ by Elbaz et al. (2002) based on a comparison of their radio-MIR versus MIR-FIR correlations. In § 3.2.2 we investigate the uncertainty in our derived L_{IR} using an independent family of model SEDs.

3.2.2. IR Bolometric Correction Uncertainty

The absolute calibration and the intrinsic uncertainty of the mid-IR to L_{IR} correlation is investigated by comparing our computed IR luminosities to those based on model SEDs of DH02. Dale and collaborators generate semiempirical 3–1100 μm model SEDs for normal star-forming galaxies. These models are created by combining three-component (large grain, very small grain, and PAH) dust emission curves based on a power-law distribution of the dust mass over heating intensity. In contrast to the CE01 family of SEDs, which are based on a combination of slightly modified empirical SEDs, these are built primarily from theoretical model emission curves in which the PAH-dominated MIR (3–12 μm) region is replaced with a modified ISOPHOT spectral component. This family of SEDs is single valued in FIR color [$f_{\nu}(60 \mu\text{m})/f_{\nu}(100 \mu\text{m})$], indicating that a galaxy IR SED can be uniquely determined with the measurement of this single FIR flux ratio.

Since we lack FIR colors, rather than try to determine the best-fit DH02 template for each galaxy, we compute L_{IR} for the entire family of SEDs, normalized to our observed $24 \mu\text{m}$ fluxes. For this comparison, we adopt the conversion

$$L_{\text{IR}}^{\text{DH}}(3\text{--}1100 \mu\text{m}) = [\zeta_1(z)\nu L_{\nu}(24 \mu\text{m}) + \zeta_2(z)\nu L_{\nu}(70 \mu\text{m}) + \zeta_3(z)\nu L_{\nu}(160 \mu\text{m})], \quad (10)$$

where the coefficients [$\zeta_1(z)$, $\zeta_2(z)$, and $\zeta_3(z)$] are taken from DH02. These SEDs represent the span of star-forming galaxy types, so the range of $L_{\text{IR}}^{\text{DH}}$ provides an estimate of the bolometric correction error due to our IR SED assumptions.

In Figure 7 (*top*), $L_{\text{IR}}^{\text{CE}}$ (L_{IR} based on CE01 templates) is plotted against the family of $L_{\text{IR}}^{\text{DH}}$ values (*dots*). The bottom panels are the residual plots shown as functions of $L_{\text{IR}}^{\text{CE}}$ (*bottom left*) and redshift (*bottom right*). The mean ratio of unity for $L_{\text{IR}}^{\text{DH}}/L_{\text{IR}}^{\text{CE}}$ indicates that the independently derived CE01 and DH02 L_{IR} values are consistent on average. The range of this ratio suggests a mean L_{IR} uncertainty of ≈ 0.2 dex for the sample as a whole and ≈ 0.3 dex for the most distant sources at $z \gtrsim 1$. At $z \approx 0.5$ the uncertainty is minimized, indicating that the $L_{\text{MIR}}\text{-}L_{\text{IR}}$ correlation is tightest for galaxies measured at rest-frame wavelengths of $\lambda \approx 15 \mu\text{m}$. It is worth noting that $L_{\text{IR}}^{\text{DH}}(3\text{--}1100 \mu\text{m})$ and $L_{\text{IR}}^{\text{CE}}(8\text{--}1000 \mu\text{m})$ are defined over different wavelength ranges; however, since the flux between 3–8 and 1000–1100 μm is of the order of a few percent of the total bolometric luminosity (DH02), this difference is ignored here.

4. AGN CONTAMINATION

The conversions of both emission-line and L_{IR} luminosity to a star formation rate hinge on the assumption that the dominant ionization and heating source is radiation from massive young stars. AGN-dominated emission-line and IR fluxes do not trace star formation and must therefore be removed from our sample. Various emission-line diagnostics such as $[\text{O III}]/\text{H}\beta$ versus $[\text{N II}]/\text{H}\alpha$ and $[\text{O III}]/\text{H}\beta$ versus $[\text{S II}]/\text{H}\alpha$ effectively separate populations with different ionization sources (Osterbrock 1989). In cases with more limited spectral coverage, individual line ratios such as $[\text{Ne III}]/[\text{O II}]$ have also been successfully used (Kobulnicky & Kewley 2004). We do not employ these line diagnostics, due to the nonuniform rest-frame spectral coverage of our sample. Instead, we rely on an IRAC color selection and the visual identification of optical spectral features to identify and remove AGN candidates from our sample.

We first flag sources with obvious AGN signatures such as broadened Balmer and/or $[\text{O II}]$ lines or strong Ne III or Ne V

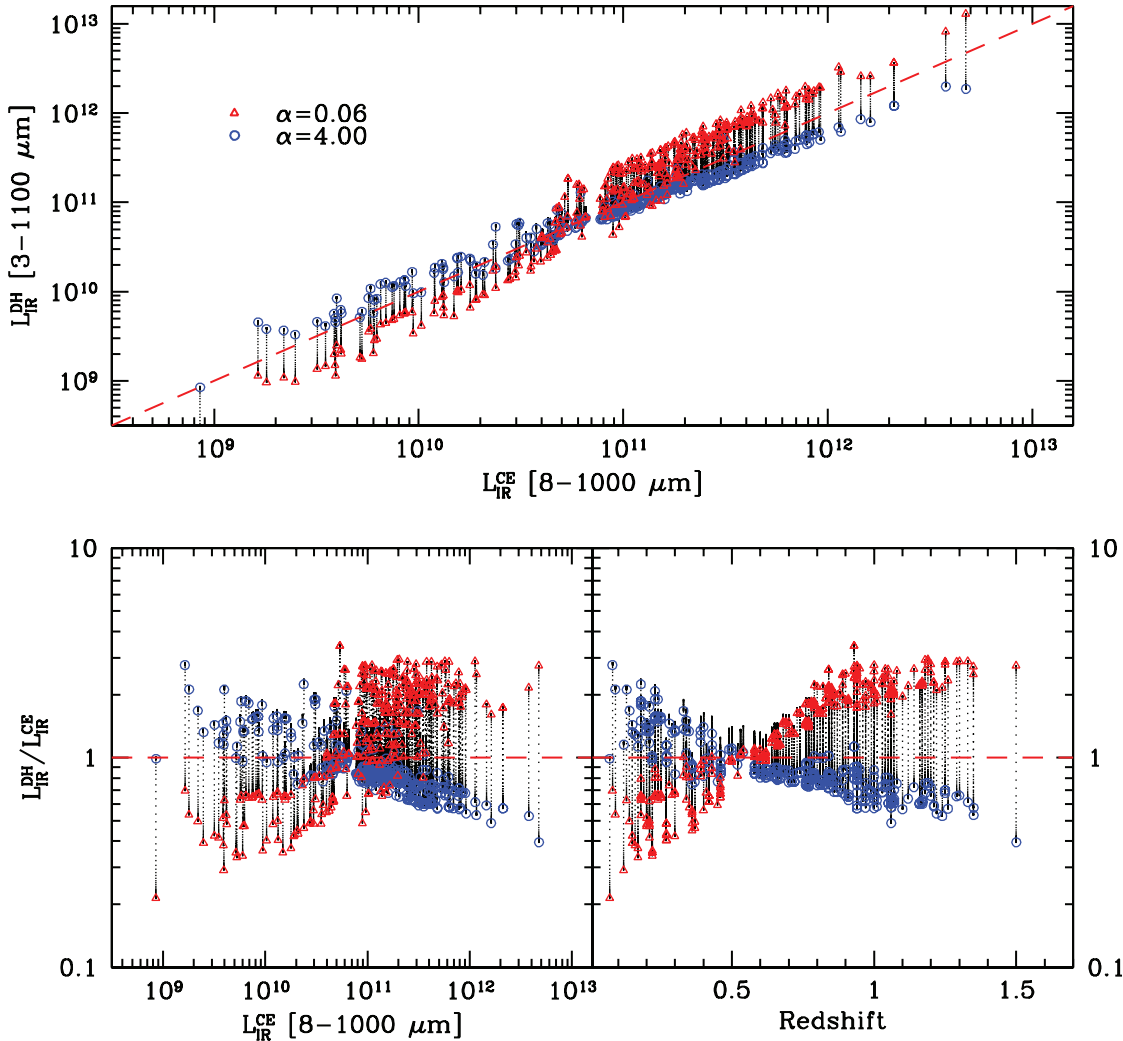


Fig. 7.—Comparison of two independent derivations of the infrared luminosity L_{IR} for sources in our sample. In the top panel, the best-fit $L_{\text{IR}}^{\text{CE}}$ for each source in our sample is compared to a range of $L_{\text{IR}}^{\text{DH}}$ computed for the full family of DH02 SEDs (black dots). Open symbols represent the limiting “hot” ($\alpha = 0.06$; red triangles) and “cold” ($\alpha = 4.00$; blue circles) DH02 SEDs. The bottom panels are residual plots shown as functions of $L_{\text{IR}}^{\text{CE}}$ (bottom left) and redshift (bottom right). This figure shows that $L_{\text{IR}}^{\text{CE}}$, adopted as our best-fit bolometric luminosity, is consistent with the range of $L_{\text{IR}}^{\text{DH}}$ that one obtains if no $L_{\text{MIR}}-L_{\text{IR}}$ correlation is assumed.

emission. Next, we combine our sample with IRAC photometry of the FLS (Lacy et al. 2005) to implement a four-band IRAC color selection. It has been shown that AGNs can be identified in the MIR, based on their strong continuum flux (Laurent et al. 2000; Lacy et al. 2004; Stern et al. 2005). Lacy et al. (2004) use four-band *Spitzer* IRAC photometry (3.6, 4.5, 5.8, and 8.0 \$\mu\text{m}\$) to identify a distinct region in color-color space where quasars and AGNs are likely to be found. In Figure 8a we reproduce the IRAC color-color plot from Lacy et al. (2004; their Fig. 1) for the entire FLS main field. The dashed line shows the region expected to be occupied by AGNs. In Figure 8b we show the same plot for our current sample. The FLS depth of the IRAC channels 3 and 4 is slightly shallower than that of channels 1 and 2, and only 2/3 of our sample have clean photometry in all four IRAC bands (open circles); for the remaining 1/3 of the sample, limiting flux ratios are shown (open triangles). Based on the IRAC color selection, 9% of each of these subsamples falls in the AGN-candidate region. Visual reinspection of the 16 IRAC-selected candidates reveals that 63% exhibit some AGN signature in their spectra (six strong; four moderate). The remaining sources show no obvious indicator; however, an AGN contribution cannot be ruled out, given our limited spectral coverage. We remove all 16 candidates from the final sample. In-

vestigation of the spectroscopically selected candidates shows that five of nine sources (55%) with strong AGN spectral signatures are also IRAC-selected AGNs. Ultimately, we find that neither the spectroscopic nor IRAC color selection provides a complete census of all AGNs, so we take the conservative approach of combining the two methods to clean our sample. The impact of this AGN removal is best illustrated in the comparison of the two different SFR diagnostics (Fig. 9), discussed in § 5.

5. OPTICAL VERSUS IR SFR COMPARISON

Next, we compare the two independently derived SFR diagnostics SFR_{opt} and SFR_{IR} described in § 3 for the full AGN-cleaned sample. In Figure 9, we show the reddening-uncorrected, emission-line-derived SFR_{opt} versus the IR luminosity-derived SFR_{IR} , before and after AGN removal. The sample plotted in Figure 9 (left) includes the 274 sources with well determined spectroscopic redshifts and emission-line and 24 \$\mu\text{m}\$ fluxes. AGN candidates are marked based on their spectral (squares) or IRAC color identification (circles; as discussed in § 4). In Figure 9 (right) only the final 241 source AGN-removed sample is shown. Although the distribution of the AGN candidates is not localized to a single region of the plot, sources with the most extreme SFR discrepancies tend to be AGNs. This illustrates the potential

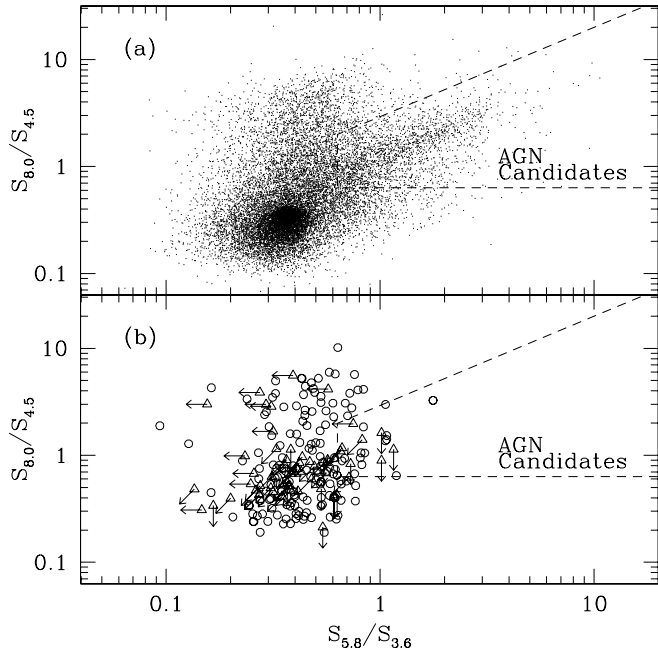


FIG. 8.—IRAC four-channel color-color plots used to identify AGN candidates. Panel (a) illustrates how the AGN candidate region of color-color space is defined by Lacy et al. (2004). All sources with clean four-color photometry from the full 4 deg² FLS main field are plotted; the region in which quasars and AGNs are expected to be found is marked by a dashed line (see Sajina et al. 2005 for details). Panel b shows our sample with the same AGN region marked. The majority of the sample ($\approx 2/3$) has clean photometry in all four IRAC bands (open circles). The remaining sources ($\approx 1/3$) have at least two measured fluxes and therefore at least one limiting color (open triangles). Sources that fall in the dashed region of this color-color diagram are flagged as AGN candidates and are removed from our final sample.

for these sources to be misidentified as heavily obscured galaxies. The inclusion of this population would bias the sample to appear overly obscured. The fact that AGN candidates are found throughout the SFR versus SFR plot is not unexpected, since the emission-line luminosity and IR luminosity are loosely correlated in AGNs.

In Figure 9 (right) the uncorrected SFR_{opt} is systematically lower than SFR_{IR} . Over the L_{IR} range of our sample, the offset spans 2 orders of magnitude and illustrates the importance of properly accounting for the optical extinction. In this section we explore a range of different extinction corrections to reconcile the two SFRs. In Figure 10, the ratio of the two diagnostics, SFR_{opt}/SFR_{IR} , is plotted to better illustrate the systematic difference between them. It is evident from Figure 10a, in which no reddening correction has been applied, that SFR_{opt} underestimates the true SFR by anywhere from 0 to 2.5 dex. In the remaining panels, we investigate the applicability of various fixed extinction corrections. In Figure 10b an extinction of $A_V = 1.0$, representative of normal spiral galaxies, is assumed. This is a significant improvement over the uncorrected SFR_{opt} , especially at low IR luminosity, typical of normal late-type galaxies. Beyond $L_{IR} > 10^{10} L_\odot$, however, the two SFRs diverge, indicating that this standard correction underestimates the attenuation in starburst and brighter galaxies. In Figures 10c and 10d we adopt more extreme corrections of $A_V = 2.0$ mag and $A_V = 3.0$ mag and find that neither provides a good solution over the full range in L_{IR} . The Calzetti et al. (2000) reddening curve is adopted for each of these corrections. We conclude that a constant A_V correction is insufficient for reconciling SFR_{opt} and SFR_{IR} . In the following sections, we take two independent approaches to characterize the optical extinction of galaxies of our sample. In § 5.1 we use Balmer decrement and other emission-line ratios to compute the extinction A_V^{em} . In § 5.2 we adopt SFR_{IR} as a proxy for

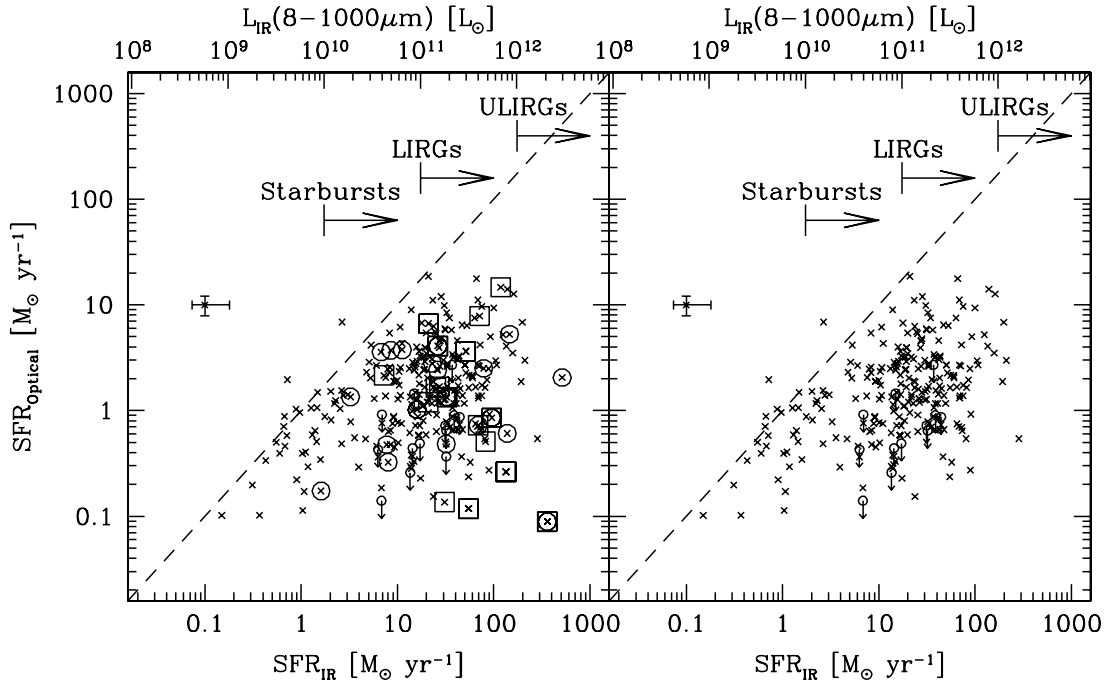


FIG. 9.—Comparison of SFR_{opt} and SFR_{IR} before (left) and after (right) AGN removal. In the left panel a sample of 274 sources with well-determined emission lines and IR luminosities is plotted as crosses. The 33 AGN candidates identified by their spectral features (squares) and IRAC colors (circles) are marked. In the right panel, the final 241 source sample after AGN removal is shown. No extinction correction has been applied to SFR_{opt} in either panel. Representative error bars are shown in each panel. The SFR_{opt} error bar is the mean 1σ uncertainty due to the error in line flux measurement. The SFR_{IR} error bar is the mean of the bolometric correction uncertainty, as discussed in § 3.2.1. The comparison of these samples illustrates (1) the importance of limiting the AGN contamination and (2) that without any reddening correction, SFR_{opt} severely underestimates the true star formation rate, especially for our most IR-luminous sources.

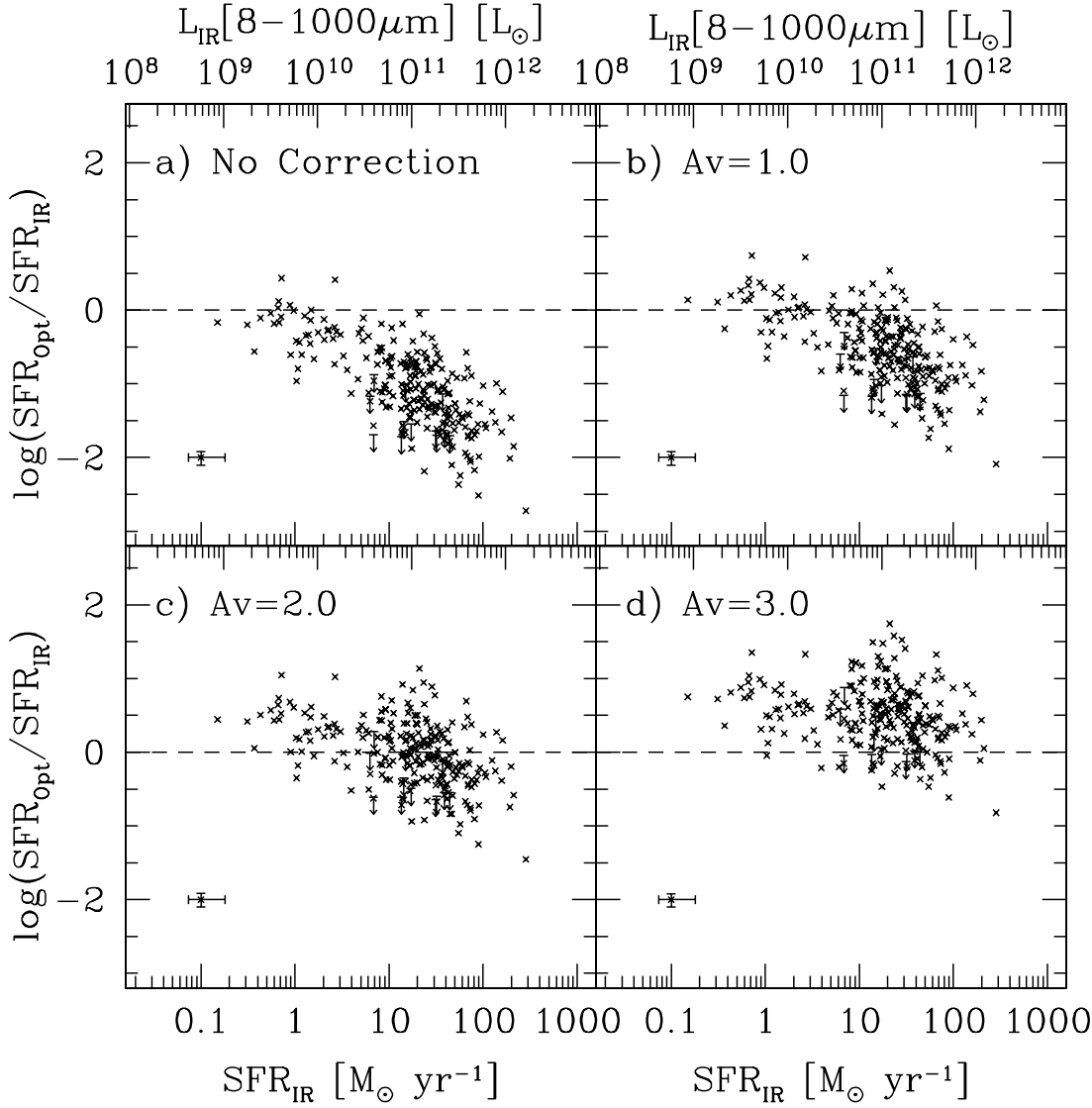


FIG. 10.— $SFR_{\text{opt}}/SFR_{\text{IR}}$ vs. SFR_{IR} and L_{IR} for the final AGN-cleaned sample, shown for a range of constant extinction corrections. In panel *a* no correction for any optical extinction is made. In panel *b* a uniform standard correction of $A_V = 1.0$ mag, typical of normal spiral galaxies, is applied to SFR_{opt} . In panels *c* and *d* more extreme constant extinction corrections, $A_V = 2.0$ mag and $A_V = 3.0$ mag, are adopted. Representative error bars are shown in each panel. The $SFR_{\text{opt}}/SFR_{\text{IR}}$ error bar includes only the mean 1σ uncertainty due to the error in line flux measurement; it does not include any uncertainty in SFR_{IR} . The SFR_{IR} error bar is the mean of the bolometric correction uncertainty, as discussed in § 3.2.1. With no extinction correction, SFR_{opt} underestimates the true star formation rate by as much as 2.5 dex for our most IR-luminous sources. Uniform extinction corrections do not adequately represent our sample of normal, starburst, and LIRG galaxies.

the true total star formation rate and compute A_V^{IR} based on the difference between SFR_{opt} and SFR_{IR} .

5.1. Optical Extinction Correction I: Balmer Decrement

A standard method for measuring the internal extinction of an individual galaxy is through the comparison of observed to predicted Balmer line ratios. We adopt this approach for the subset of our sample with multiple measured Balmer lines. The color excess $E(B-V)_{\text{gas}}$ of a source is computed by comparing the observed Balmer line ratios ($F_o^{\text{H}\alpha}/F_o^{\text{H}\beta}$), ($F_o^{\text{H}\delta}/F_o^{\text{H}\beta}$), and ($F_o^{\text{H}\gamma}/F_o^{\text{H}\beta}$) with their intrinsic unobscured ratios,

$$E(B-V)_{\text{gas}} = \frac{2.5}{[k(\lambda_1) - k(\lambda_2)]} \log \frac{(F_i^{\lambda_1}/F_i^{\lambda_2})}{(F_o^{\lambda_1}/F_o^{\lambda_2})}, \quad (11)$$

where $F_i^{\lambda_1}/F_i^{\lambda_2}$ are the intrinsic unobscured line ratios based on case B recombination and $T = 10,000$ K (Osterbrock 1989).

The obscuration or reddening curve [$k(\lambda)$] has been derived by Calzetti et al. (2000) for starburst galaxies as

$$k(\lambda) = \begin{cases} 2.659 \left(-1.857 + \frac{1.040}{\lambda} \right) \\ + R_V, & 0.63 \leq \lambda \leq 2.20 \mu\text{m}, \\ 2.659 \left(-2.156 + \frac{1.509}{\lambda} \right) \\ - \frac{0.198}{\lambda^2} + \frac{0.011}{\lambda^3} \right) + R_V, & 0.12 \leq \lambda \leq 0.63 \mu\text{m}. \end{cases} \quad (12)$$

It should be noted that although there are significant large-scale differences between the various starburst, Milky Way, LMC, and SMC reddening curves, over the rest-frame spectral region covered by the emission lines of interest ($3700 \text{ \AA} \leq \lambda \leq 6600 \text{ \AA}$),

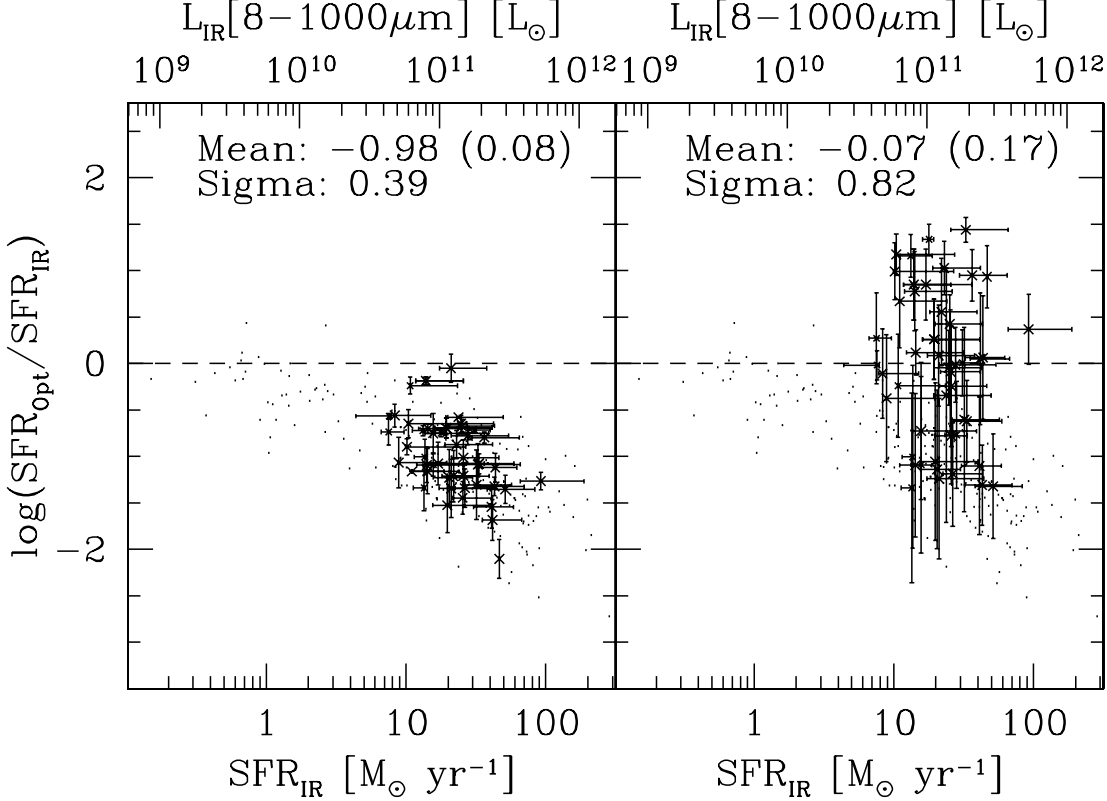


FIG. 11.— $SFR_{\text{opt}}/SFR_{\text{IR}}$ vs. SFR_{IR} and L_{IR} before and after application of *emission-line-ratio*-derived reddening corrections A_V^{em} . A sample of 24 sources is shown (*crosses*) before (*left*) and after (*right*) the application of A_V^{em} . For reference, the full sample is also plotted (*small dots*). The SFR_{IR} error bars represent the full range of the bolometric correction uncertainty, as discussed in § 3.2.2. The $SFR_{\text{opt}}/SFR_{\text{IR}}$ error bars show the 1σ uncertainty due to the error in line flux measurement, excluding any contribution from SFR_{IR} . In the right panel, individual y -error bars also include the uncertainty in A_V^{em} . Application of A_V^{em} results in a reasonable *ensemble-averaged* SFR, as evidenced by the improvement of $\langle \log(SFR_{\text{opt}}/SFR_{\text{IR}}) \rangle$ from -0.98 to -0.07 . However, the significant increase in scatter suggests that our emission-line ratios do not provide optimal corrections for individual sources.

the differences are minor (Calzetti 2001 and references therein). The color excess is converted into a wavelength-dependent extinction based on

$$A(\lambda) = E(B-V)_{\text{gas}} k(\lambda), \quad (13)$$

where $A(\lambda)$ is the mean emission-line-derived extinction in units of magnitudes at the wavelength λ . This should be distinguished from $A_s(\lambda)$, the extinction as measured from the stellar continuum. As has been shown by Calzetti (2001), these differ by a factor of 0.44 in typical local starbursts.

In addition to using the Balmer decrement, we explore the possibility of using the $[\text{O II}]/\text{H}\beta$ line ratio to compute A_V^{em} . Although this ratio is less certain than that of the Balmer lines, we adopt an empirical value for the intrinsic $[\text{O II}]/\text{H}\beta$ line ratio based on the locally measured reddening-corrected line fluxes. Using the NFGS, Kewley et al. (2004) measure a mean extinction-corrected $[\text{O II}]/\text{H}\alpha$ ratio of 1.2, which translates to an $[\text{O II}]/\text{H}\beta$ line ratio of

$$F_i^{[\text{O II}]} / F_i^{\text{H}\beta} = 3.44.$$

From our full sample, individual reddening corrections A_V^{em} are computed for 24 sources that have multiple strong Balmer and/or $[\text{O II}]$ emission lines. Line fluxes and SFR_{opt} are then reddening corrected on a source-by-source basis. In Figure 11, $SFR_{\text{opt}}/SFR_{\text{IR}}$ versus SFR_{IR} for this sample (*crosses*) is shown before (*left*) and after (*right*) application of this correction. There is a significant increase in the scatter of the distribution after application of the

extinction correction. This illustrates that due to the enormous uncertainties associated with A_V^{em} , source-by-source corrections are futile. Despite the increased scatter, it is noteworthy that SFR_{opt} becomes consistent on average with SFR_{IR} , with the mean offset reduced from -0.98 to -0.07 dex. This indicates that in the absence of other extinction indicators, with a large enough sample and careful stellar absorption measurements, Balmer decrement and $[\text{O II}]/\text{H}\beta$ emission-line ratios can provide a reasonable first-order $\langle A_V^{\text{em}} \rangle$ correction for the luminosity range of this sample. The median emission-line-derived extinction of this subsample is $A_V^{\text{em}} = 1.5 \pm 1.1$ mag with $\langle SFR_{\text{IR}} \rangle = 23 \pm 8 M_{\odot} \text{yr}^{-1}$. Due to the relatively small size and limited L_{IR} coverage of this subsample, along with the large uncertainties, we are not able to derive an L_{IR} -dependent extinction correction. Instead, in § 5.2 we adopt SFR_{IR} as a “true” SFR and compare it to the extinction-uncorrected SFR_{opt} to derive A_V^{IR} for the full sample.

5.2. Optical Extinction Correction II: IR versus Optical SFRs

5.2.1. Computing A_V^{IR}

In this section, we take an alternative approach of adopting SFR_{IR} as a proxy for the true SFR to determine the extinction correction of our sample. Specifically, the ratio SFR_{IR} over the uncorrected SFR_{opt} is used to compute the attenuation of the given emission line,

$$A(\lambda) = -2.5 \log(SFR_{\text{opt}}/SFR_{\text{IR}}), \quad (14)$$

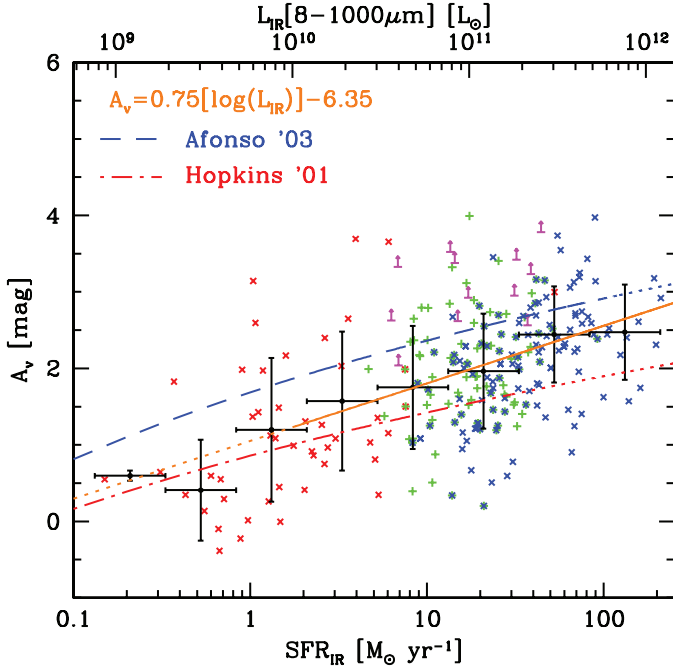


FIG. 12.—Optical extinction A_V^{IR} vs. L_{IR} for the complete galaxy sample. Here A_V^{IR} is derived from the ratio of $\text{SFR}_{\text{opt}}/\text{SFR}_{\text{IR}}$, where SFR_{IR} is adopted as a proxy for the true SFR, and plotted as a function of IR luminosity (crosses and plus signs). Sources with measured H α , H β , and [O II] line fluxes are shown as red, green, and blue points, respectively. Those with only emission-line flux limits are shown as magenta arrows. Mean A_V^{IR} values (solid circles), binned in log (SFR_{IR}), are plotted along with their 1σ uncertainties. The best-fit line $A_V^{\text{IR}} = 0.75 \log(L_{\text{IR}}/L_\odot) - 6.35$ mag is computed and overlaid as a solid orange line and compared to those derived by H01 (dot-dashed red line) and A03 (dashed blue line). Extrapolations beyond the data set luminosity limits are indicated by dotted lines. The mean measured A_V^{IR} function of our sample is intermediate between those of H01 and A03, with evidence for a stronger L_{IR} dependence.

where λ is the wavelength of the emission line used to compute SFR_{opt} . Here $A(\lambda)$ is converted to a standard visual extinction A_V by

$$A_V = \frac{A(\lambda)}{k(\lambda)} k_V. \quad (15)$$

The extinction derived in this manner may have a large uncertainty for individual sources, but this approach should produce a reasonable ensemble average. In Figure 12, A_V^{IR} versus SFR_{IR} and L_{IR} is shown for our full sample. Despite the large scatter in the distribution, a clear trend of increasing A_V^{IR} as a function of SFR_{IR} is evident. The best-fit line to this distribution is

$$A_V^{\text{IR}} = 0.75 \log(\text{SFR}_{\text{IR}}) + 1.05, \quad (16)$$

which in terms of L_{IR} is

$$A_V^{\text{IR}} = 0.75 \log(L_{\text{IR}}/L_\odot) - 6.35. \quad (17)$$

This fit is limited to starburst and brighter systems ($L_{\text{IR}} > 10^{10} L_\odot$; Fig. 12, orange solid line), where SFR_{IR} is a good representation of the total SFR. It is extrapolated to lower luminosities ($L_{\text{IR}} < 10^{10} L_\odot$; orange dotted line). Inclusion of the full sample has only a minor effect, slightly steepening the fit. The mean A_V^{IR} values (black dots) of sources binned in log (SFR_{IR}) are overlaid along with error bars that show their 1σ dispersion.

5.2.2. Comparison to Local Samples

We now make a direct comparison of our A_V^{IR} function to those of local optical/UV- (Hopkins et al. 2001, hereafter H01) and radio-selected samples of Afonso et al. (2003, hereafter A03). We transform their $E(B-V)$ color excess to A_V based on $R_V = 3.1$ and overplot them in Figure 12 as red dot-dashed and blue dashed curves, with dotted segments representing extrapolations beyond their data sets. For a given SFR, the mean A_V^{IR} of our sample is intermediate between those of H01 and A03. The trend in the extinction as a function of L_{IR} is also slightly steeper than the previous relationships. This can be seen in Figure 13, which shows a comparison of the various extinction functions applied to our AGN-cleaned final sample. To interpret these differences requires a closer examination of the various sample selections.

The H01 SFR-dependent extinction relationship is based on small ($N \approx 60$) local UV + optical-selected samples (cf. Sullivan et al. 2001), whereas that of A03 is derived from a comparably sized radio-selected sample that extends to slightly higher redshift $\langle z \rangle \approx 0.25$ and is more actively star forming. The difference in the mean A_V between the two samples is attributed to the fact that optical/UV-selected samples are biased against heavily obscured galaxies. Our initial spectroscopic sample is NIR-selected ($2.2 \mu\text{m}$), so compared to a UV/optical sample, we expect it to be significantly less affected by obscuration effects. It is therefore not surprising that our mean A_V^{IR} is higher than that of H01.

The discrepancy between our sample and that of A03 is more difficult to understand, since both radio and NIR/MIR selections should be relatively robust against obscuration biases. It is suggestive of a selection bias in one or both samples. Reliance on optical spectroscopy may be one potential culprit. It is possible that the dustiest systems are so heavily obscured that either their redshifts are indeterminable or their emission lines are completely attenuated. We can place some constraints on the sizes of these two populations in our sample. Our spectroscopic redshift efficiency of $92\% \pm 5\%$ places an 8% limit on the first. This is a conservative estimate, since some fraction of the 8% is certainly due to our spectroscopic redshift sensitivity function dropping off beyond $z \approx 1.3$. Regarding the second population, 12 sources in our sample (<4%) with identified redshifts have no measured emission-line fluxes and therefore only lower limits on the derived attenuation. These are shown as arrows in Figures 9 and 12 and are included in our $A_V^{\text{IR}}(L_{\text{IR}})$ estimate. Deeper optical spectroscopy may reveal these to be even more heavily obscured systems. Based on these estimates, these two populations are likely to account for $\lesssim 10\%$ of the total population. It is worth noting that these biases are not unique to this study, since most surveys rely on optical spectroscopy for redshift and/or emission-line diagnostics.

One potential bias that may *overestimate* the mean optical attenuation is due to AGN contamination. Especially in the most luminous samples, the contribution from AGNs becomes increasingly significant. Radio-selected and, to a lesser extent, MIR-selected samples will tend to have larger fractions of “active” galaxies than comparable depth optical or NIR samples. As seen in Figure 9, if this population is not sufficiently screened, they can result in an overestimate of the sample A_V .

Finally, our A_V^{IR} values appear to be consistent with those derived from an SDSS sample of star-forming galaxies (Hopkins et al. 2003). Although no direct comparison is shown here, inspection of their Figure 8 shows that the mean A_V of their sample is intermediate between that of H01 and A03, consistent with the correction derived here over a comparable range of SFR.

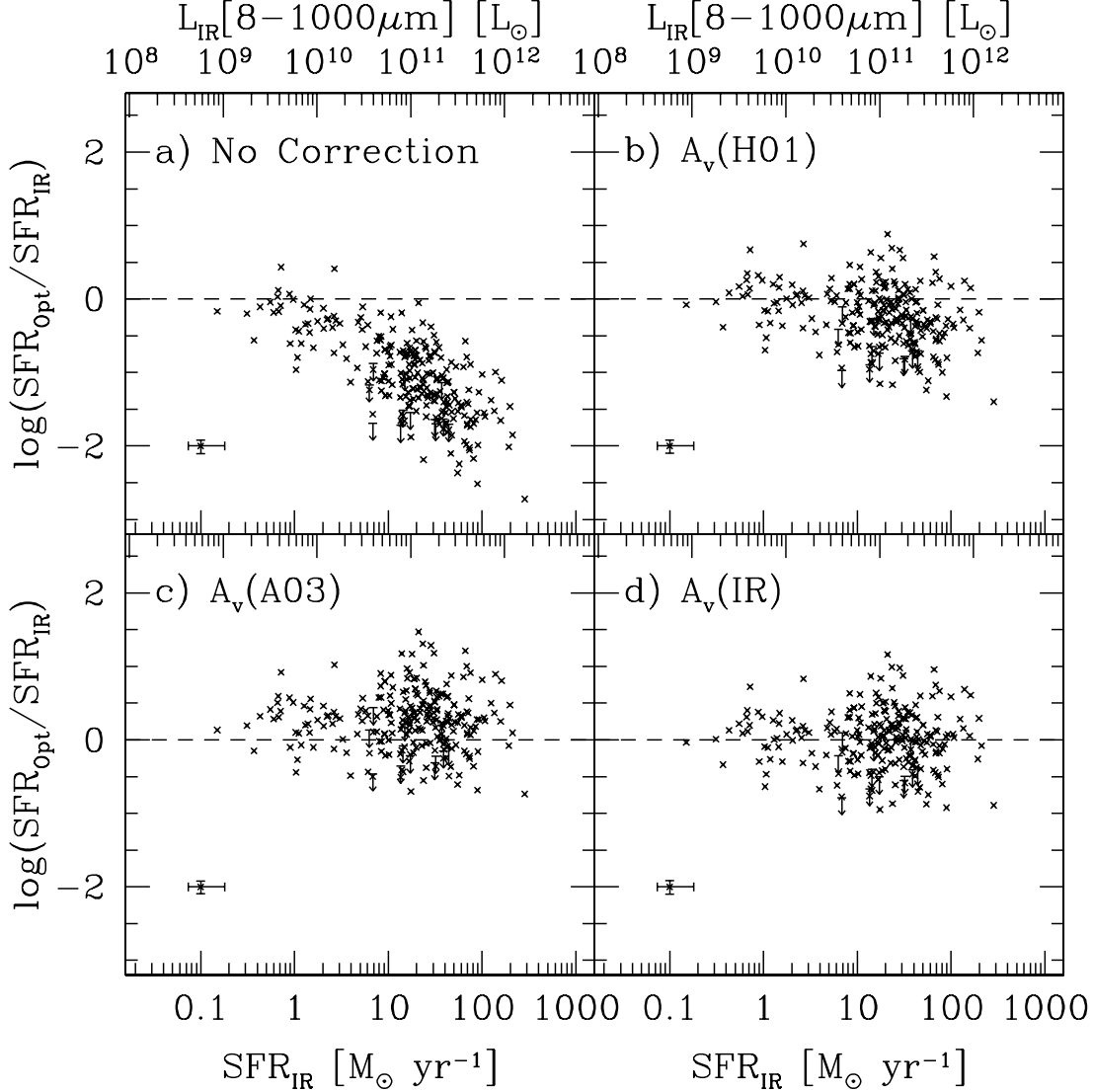


FIG. 13.— $SFR_{\text{opt}}/SFR_{\text{IR}}$ vs. SFR_{IR} and L_{IR} of the final AGN-cleaned sample, with various luminosity-dependent extinction corrections. In panel *a* no correction for any optical extinction is made. In panels *b* and *c* we adopted the A_V functions derived by H01 and A03, respectively. In panel *d* we adopt our best-fit A_V^{IR} extinction function based on our sample. Representative error bars are the same as in Fig. 10. We see that the corrections of H01 and A03 appear to underestimate and overestimate the mean extinction of our sample, respectively. The scatter of the corrected sample in panel *d* is 0.3 dex.

5.2.3. Disentangling the L_{IR} versus Redshift Dependence

As seen in Figure 6, our sample spans a broad range in both IR luminosity and redshift, and as a consequence of our 24 μm flux limit it exhibits a strong L_{IR} -redshift correlation. So far, we have been assuming that for a fixed L_{IR} , A_V is largely redshift independent. Given the potential degeneracy between redshift and IR luminosity dependencies, the validity of this assumption merits investigation.

Although our sample is not ideally suited for a thorough study of this issue, we can place some limits on the redshift dependence by isolating subsets of our data restricted in IR luminosity and redshift. In Figure 14, we take a look at two such slices in L_{IR} and redshift. The first is restricted to $2 \times 10^{11} < L_{\text{IR}}/L_{\odot} < 1 \times 10^{12}$, and the second to $0.7 < z < 1.0$. In the bottom panels, plots of A_V versus redshift and A_V versus L_{IR} for the respective subsets reveal that (1) for a sample with a narrow range of L_{IR} , there is no strong trend in A_V with redshift, and (2) over a relatively narrow redshift slice centered at $z = 0.85$, A_V shows a clear correlation with L_{IR} . Although our sample does not allow

us to investigate trends over the entire redshift or L_{IR} range of our sample, these two slices suggest that to first order the dependence on redshift is small compared to that on L_{IR} .

6. SUMMARY

We have combined MIR (24 μm) photometry with high-resolution optical spectroscopy for a large ($N = 241$), $K_s +$ MIPS 24 μm -selected ($K_s < 20.2$ mag; $f_{24} > 80 \mu\text{Jy}$) galaxy sample. AGNs are removed by implementing both spectroscopic and MIR color selections. This data set is used to measure the instantaneous star formation rate and the mean attenuation of normal through IR-luminous galaxies ($10^9 < L_{\text{IR}} < 10^{12.5} L_{\odot}$, $\langle L_{\text{IR}} \rangle = 1.8 \times 10^{11} L_{\odot}$, and $\langle \text{SFR} \rangle = 31 M_{\odot} \text{ yr}^{-1}$) out to a redshift of $z < 1.5$ ($\langle z \rangle = 0.77$). We compare two independent approaches to computing the star formation rate. The first is based on the IR luminosity, SFR_{IR} , and the second is based on optical Balmer and [O II] emission-line fluxes, SFR_{opt} .

Comparison of the two SFR diagnostics reveals that with no correction for extinction, the optical SFR systematically

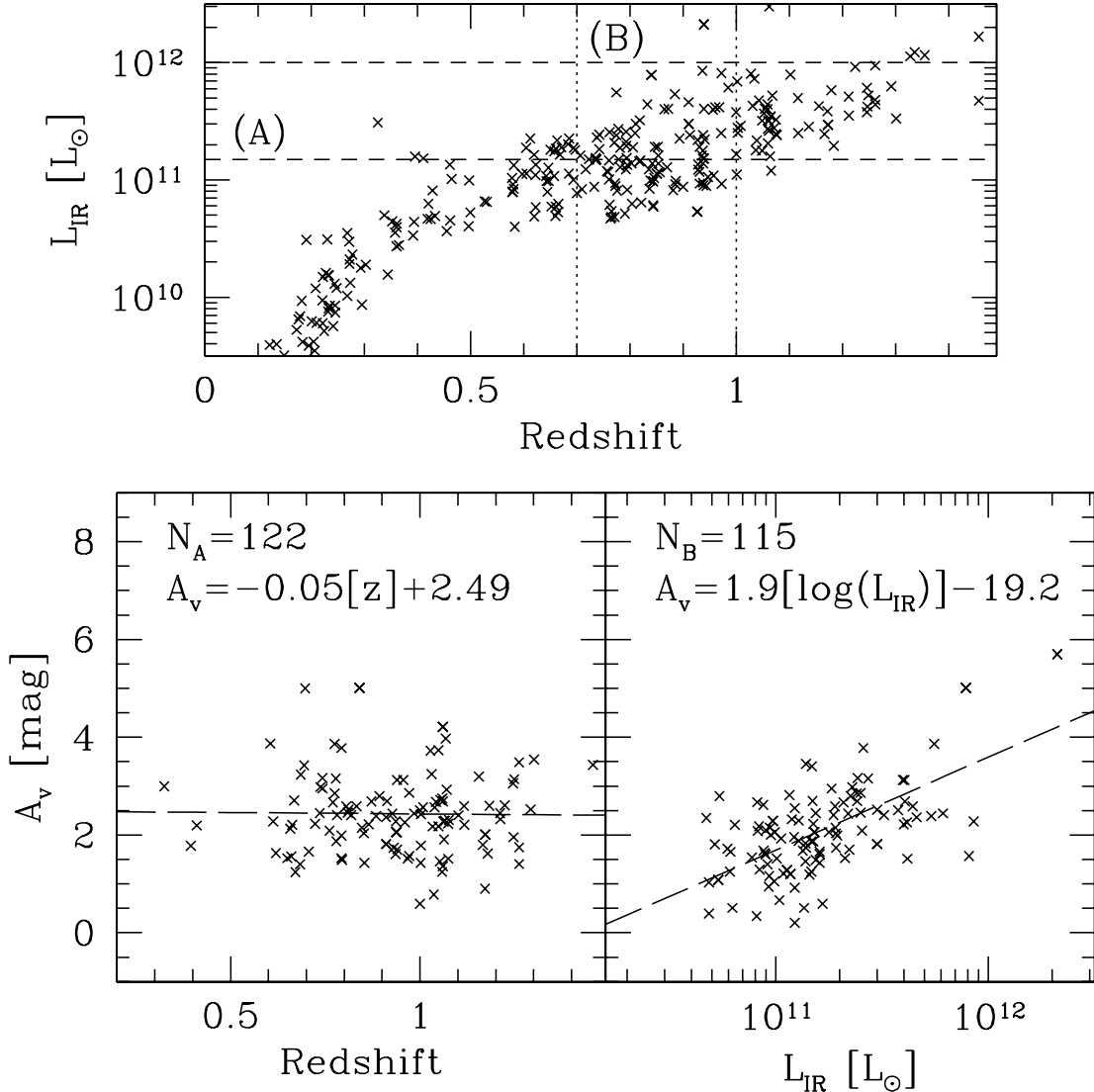


FIG. 14.—Comparison of the A_V^{IR} dependence on IR luminosity and redshift for two subsets of our final sample. In the L_{IR} vs. redshift plot (top), two regions limited in L_{IR} ($2 \times 10^{11} < L_{\text{IR}} < 1 \times 10^{12}$) and redshift ($0.7 < z < 1.0$) are identified with dashed and dotted lines and marked A and B, respectively. The bottom panels show A_V^{IR} vs. redshift for 122 galaxies from region A (bottom left) and A_V^{IR} vs. L_{IR} for 115 galaxies from region B (bottom right). The bottom left panel reveals that for a fixed L_{IR} , A_V exhibits almost no redshift dependence. By contrast, the bottom right panel shows that even over a narrow redshift range, A_V has a clear L_{IR} dependence.

underestimates the IR SFR by as much as 2.5 dex. This discrepancy has a clear IR luminosity dependence that cannot be reconciled with a constant A_V extinction correction. We take two independent approaches to investigate the dust attenuation of our sample.

First, we compute the Balmer decrement– and emission-line-ratio–derived optical extinction A_V^{em} on a source-by-source basis for a subset of our sample. We find that after correction, despite a large scatter in the distribution, the ensemble averaged SFR_{opt} is consistent with SFR_{IR} . The large errors associated with the derived A_V^{em} , however, illustrate that even with the stellar continuum properly measured, the high-order Balmer line ratios, such as $H\beta/H\gamma$ and $H\beta/H\delta$, as well as $[\text{O II}]/H\beta$, have only a limited usefulness for extinction corrections of individual galaxies at high redshift. This is due to (1) the relative weakness of these high order emission lines and (2) the limited leverage afforded by the narrow separation of these lines, in comparison to the conventionally adopted $\text{H}\alpha/\text{H}\beta$ Balmer decrement.

As an alternative measure of the optical attenuation, we use $\text{SFR}_{\text{opt}}/\text{SFR}_{\text{IR}}$ to derive an IR-luminosity-dependent extinction

function, $A_V^{\text{IR}} = 0.75 \log(L_{\text{IR}}/L_{\odot}) - 6.35$ mag. In comparing this relationship with local optical/UV- and radio-selected samples, we find that our A_V^{IR} function is intermediate between those of H01, Sullivan et al. (2001), and A03, but with a slightly steeper slope. Although it is difficult to reconcile these results without a directly overlapping sample, we highlight some of the key differences that may contribute to the discrepancy. A03 suggest that the difference between their results is due to selection bias against highly obscured objects in the original H01 sample. Our sample should be relatively free of this selection bias and therefore comparable to that of A03. The fact that they are not is a bit surprising, but may suggest that one or both of these samples is still suffering from an additional bias. One possibility is that we may be excluding the most highly obscured sources due to our spectroscopic sensitivities. This is not likely to have a dominant effect given the high 92% spectroscopic redshift efficiency of our sample and the fact that all spectroscopic samples are affected by this bias. Another possibility is that the A03 sample, due to its radio-selected nature, may contain a larger fraction of galaxies with an AGN that may be inflating their mean A_V . The

inclusion of even nondominant AGNs may have a similar effect on the measured ensemble extinction to that of a heavily dust-obscured population.

We do not attempt to quantify the A_V evolution over our full redshift range. However, based on subsamples restricted to narrow redshift and L_{IR} ranges, we find no evidence for significant A_V evolution.

The scatter in $\text{SFR}_{\text{opt}}/\text{SFR}_{\text{IR}}$ after application of our best-fit attenuation correction is larger than expected from either the line flux errors or the reasonable estimates of the IR bolometric correction uncertainty. The impact of adopting a mean metallicity correction ($\lesssim 0.1$ dex) also cannot account for this scatter. This indicates that these diagnostics are not providing consistent tracers of the current SFR, possibly due to differences in their dependence on dust geometry and/or SFR timescale.

We thank the anonymous referee for insightful comments that have significantly improved this paper. We thank Dave

Thomson for his contribution to the observation and reduction of the WIRC data. We would also like to thank Carol Lonsdale, Robert Kennicutt, and Rolf Jansen for early discussions that helped shape this project. This work is based (in part) on observations made with the *Spitzer Space Telescope*, which is operated by the Jet Propulsion Laboratory, California Institute of Technology under a contract with NASA. Support for this work was provided by NASA through an award issued by JPL, Caltech. M. I. was supported by grant R01-2005-000-10610-0 from the Basic Research Program of the Korea Science and Engineering Foundation. We are indebted to Grant Hill, Greg Wirth, and the rest of the Keck observatory staff for their phenomenal observation support. The analysis pipeline used to reduce the DEIMOS data was developed by the DEEP2 group at UC Berkeley with support from NSF grant AST 00-71048. Finally, we wish to recognize and acknowledge the significant cultural role and reverence that the summit of Mauna Kea has within the indigenous Hawaiian community. We are grateful for the opportunity to conduct observations from this mountain.

REFERENCES

- Adelberger, K. L., & Steidel, C. C. 2000, ApJ, 544, 218
 Afonso, J., Hopkins, A., Mobasher, B., & Almeida, C. 2003, ApJ, 597, 269 (A03)
 Bell, E. F. 2002, ApJ, 577, 150
 ———. 2003, ApJ, 586, 794
 Bell, E. F., Gordon, K. D., Kennicutt, R. C., & Zaritsky, D. 2002, ApJ, 565, 994
 Bell, E. F., & Kennicutt, R. C. 2001, ApJ, 548, 681
 Blanton, M. R., et al. 2003, AJ, 125, 2348
 Buat, V., Boselli, A., Gavazzi, G., & Bonfanti, C. 2002, A&A, 383, 801
 Calzetti, D. 2001, PASP, 113, 1449
 Calzetti, D., Armus, L., Bohlin, R. C., Kinney, A. L., Koornneef, J., & Storchi-Bergmann, T. 2000, ApJ, 533, 682
 Calzetti, D., Kinney, A. L., & Storchi-Bergmann, T. 1994, ApJ, 429, 582
 Cardiel, N., Elbaz, D., Schiavon, R. P., Willmer, C. N. A., Koo, D. C., Phillips, A. C., & Gallego, J. 2003, ApJ, 584, 76
 Chary, R., & Elbaz, D. 2001, ApJ, 556, 562 (CE01)
 Condon, J. J. 1992, ARA&A, 30, 575
 Cram, L., Hopkins, A., Mobasher, B., & Rowan-Robinson, M. 1998, ApJ, 507, 155
 Dale, D. A., & Helou, G. 2002, ApJ, 576, 159 (DH02)
 Desert, F.-X., Boulanger, F., & Puget, J. L. 1990, A&A, 237, 215
 Diolaiti, E., Bendinelli, O., Bonaccini, D., Close, L., Currie, D., & Parmeggiani, G. 2000, A&AS, 147, 335
 Dopita, M. A., Pereira, M., Kewley, L. J., & Capaccioli, M. 2002, ApJS, 143, 47
 Elbaz, D., Cesarsky, C. J., Chanial, P., Aussel, H., Franceschini, A., Fadda, D., & Chary, R. R. 2002, A&A, 384, 848
 Erb, D. K., Shapley, A. E., Steidel, C. C., Pettini, M., Adelberger, K. L., Hunt, M. P., Moorwood, A. F. M., & Cuby, J. 2003, ApJ, 591, 101
 Faber, S. M., et al. 2003, Proc. SPIE, 4841, 1657
 Fadda, D., Jannuzzi, B. T., Ford, A., & Storrie-Lombardi, L. J. 2004, AJ, 128, 1
 Fazio, G. G., et al. 2004, ApJS, 154, 10
 Flores, H., Hammer, F., Elbaz, D., Cesarsky, C. J., Liang, Y. C., Fadda, D., & Gruel, N. 2004, A&A, 415, 885
 Gallagher, J. S., Hunter, D. A., & Bushouse, H. 1989, AJ, 97, 700
 Ghosh, P., & White, N. E. 2001, ApJ, 559, L97
 Glazebrook, K., Blake, C., Economou, F., Lilly, S., & Colless, M. 1999, MNRAS, 306, 843
 Goldader, J. D., Meurer, G., Heckman, T. M., Seibert, M., Sanders, D. B., Calzetti, D., & Steidel, C. C. 2002, ApJ, 568, 651
 Helou, G. 2000, in Infrared Space Astronomy, Today and Tomorrow, ed. F. Casoli, J. Lequeux, & F. David (Berlin: Springer), 337
 Helou, G., & Bicay, M. D. 1993, ApJ, 415, 93
 Helou, G., Soifer, B. T., & Rowan-Robinson, M. 1985, ApJ, 298, L7
 Hippelstein, H., et al. 2003, A&A, 402, 65
 Hogg, D. W., Cohen, J. G., Blandford, R., & Pahre, M. A. 1998, ApJ, 504, 622
 Hopkins, A. M., Connolly, A. J., Haarsma, D. B., & Cram, L. E. 2001, AJ, 122, 288 (H01)
 Hopkins, A. M., et al. 2003, ApJ, 599, 971
 Kennicutt, R. C. 1992, ApJS, 79, 255
 ———. 1998, ARA&A, 36, 189
 Kewley, L. J., Geller, M. J., & Jansen, R. A. 2004, AJ, 127, 2002
 Kewley, L. J., Geller, M. J., Jansen, R. A., & Dopita, M. A. 2002, AJ, 124, 3135
 Kobulnicky, H. A., & Kewley, L. J. 2004, ApJ, 617, 240
 Lacy, M., et al. 2004, ApJS, 154, 166
 ———. 2005, ApJS, 161, 41
 Laurent, O., Mirabel, I. F., Charmandaris, V., Gallais, P., Madden, S. C., Sauvage, M., Vigroux, L., & Cesarsky, C. 2000, A&A, 359, 887
 Lonsdale-Persson, C. J., & Helou, G. 1987, ApJ, 314, 513
 Maddalena, P., Ferguson, H. C., Dickinson, M. E., Giavalisco, M., Steidel, C. C., & Fruchter, A. 1996, MNRAS, 283, 1388
 Marleau, F. R., et al. 2004, ApJS, 154, 66
 McGaugh, S. S. 1991, ApJ, 380, 140
 Osterbrock, D. E. 1989, Astrophysics of Gaseous Nebulae and Active Galactic Nuclei (Mill Valley: University Science Books)
 Rieke, G. H., et al. 2004, ApJS, 154, 25
 Rigopoulou, D., et al. 2000, ApJ, 537, L85
 Sajina, A., Lacy, M., & Scott, D. 2005, ApJ, 621, 256
 Sanders, D. B., & Mirabel, I. F. 1996, ARA&A, 34, 749
 Silva, L., Granato, G. L., Bressan, A., & Danese, L. 1998, ApJ, 509, 103
 Stern, D., et al. 2005, ApJ, 631, 163
 Sullivan, M., Mobasher, B., Chan, B., Cram, L., Ellis, R., Treyer, M., & Hopkins, A. 2001, ApJ, 558, 72
 Sullivan, M., Treyer, M. A., Ellis, R. S., & Mobasher, B. 2004, MNRAS, 350, 21
 Takeuchi, T. T., Buat, V., Iglesias-Páramo, J., Boselli, A., & Burgarella, D. 2005, A&A, 432, 423
 Teplitz, H. I., Collins, N. R., Gardner, J. P., Hill, R. S., & Rhodes, J. 2003, ApJ, 589, 704
 Tresse, L., & Maddox, S. J. 1998, ApJ, 495, 691
 Wilson, G., Cowie, L. L., Barger, A. J., & Burke, D. J. 2002, AJ, 124, 1258
 Yan, L., McCarthy, P. J., Freudling, W., Teplitz, H. I., Malumuth, E. M., Weymann, R. J., & Malkan, M. A. 1999, ApJ, 519, L47